

2013

Modeling and eddy simulation of rotating and curved turbulent flows

Sunil Kumar Arolla
Iowa State University

Follow this and additional works at: <https://lib.dr.iastate.edu/etd>

 Part of the [Aerospace Engineering Commons](#)

Recommended Citation

Arolla, Sunil Kumar, "Modeling and eddy simulation of rotating and curved turbulent flows" (2013). *Graduate Theses and Dissertations*. 13092.

<https://lib.dr.iastate.edu/etd/13092>

This Dissertation is brought to you for free and open access by the Iowa State University Capstones, Theses and Dissertations at Iowa State University Digital Repository. It has been accepted for inclusion in Graduate Theses and Dissertations by an authorized administrator of Iowa State University Digital Repository. For more information, please contact digirep@iastate.edu.

Modeling and eddy simulation of rotating and curved turbulent flows

by

Sunil Kumar Arolla

A dissertation submitted to the graduate faculty
in partial fulfillment of the requirements for the degree of
DOCTOR OF PHILOSOPHY

Major: Aerospace Engineering

Program of Study Committee:

Paul A. Durbin, Major Professor

Alric Rothmayer

Thomas J. Rudolphi

Shankar Subramaniam

Song-Charng Kong

Iowa State University

Ames, Iowa

2013

Copyright © Sunil Kumar Arolla, 2013. All rights reserved.

DEDICATION

To my parents and sister

TABLE OF CONTENTS

LIST OF TABLES	vi
LIST OF FIGURES	vii
ACKNOWLEDGEMENTS	x
ABSTRACT	xi
CHAPTER 1. GENERAL INTRODUCTION	1
1.1 Background	1
1.2 Original contributions of this dissertation	3
CHAPTER 2. MODELING ROTATION AND CURVATURE EFFECTS	
WITHIN SCALAR EDDY VISCOSITY MODEL FRAMEWORK .	4
2.1 Abstract	4
2.2 Introduction	4
2.3 Analysis of the Second Moment Closures	7
2.3.1 Analogy between rotation and curvature	7
2.3.2 Bifurcation analysis: Combined effects of rotation and curvature .	9
2.4 Scalar eddy viscosity model framework	11
2.4.1 Bifurcation approach	12
2.4.2 Modified coefficients approach	17
2.4.3 Unification of rotation and curvature	18
2.5 Numerical implementation in a finite volume CFD code	19
2.5.1 Toy problem 1: Lamb-Oseen vortex	21

2.5.2	Toy problem 2: Lamb-Oseen vortex with an axial component . . .	22
2.5.3	Numerical issues	22
2.6	Results and discussion	23
2.6.1	Rotating Plane Channel	23
2.6.2	Curved wall boundary layer	26
2.6.3	Hydrocyclone	29
2.6.4	Serpentine Channel	31
2.6.5	Rotating Backward-facing step	35
2.6.6	Rotating serpentine channel	37
2.6.7	Rotating U-duct	38
2.6.8	Circulation control airfoil	44
2.6.9	Tip leakage vortex	47
CHAPTER 3. GENERATING INFLOW TURBULENCE FOR EDDY		
SIMULATION OF TURBOMACHINERY FLOWS		
3.1	Abstract	54
3.2	Introduction	54
3.3	Recycling and rescaling method	57
3.3.1	Simplified method with modifications due to Spalart <i>et al.</i> (2006)	59
3.3.2	Modifications due to Jewkes <i>et al.</i> (2011)	59
3.4	Validation	61
3.4.1	Flat plate boundary layer	61
3.4.2	Flow through channel	65
3.4.3	Flow through annulus	66
3.4.4	Turbine transition duct	67
3.5	Future scope of work	71
3.5.1	Algorithm enhancements	71
3.5.2	Applications	72

CHAPTER 4. GENERAL CONCLUSIONS	73
4.1 Modeling rotation and curvature effects within scalar eddy viscosity model framework	73
4.2 Generating inflow turbulence for eddy simulation of turbomachinery flows	74
BIBLIOGRAPHY	75

LIST OF TABLES

2.1	Comparison of salient points on the bifurcation diagram. \mathcal{S} is shear rate	15
2.2	Salient points on the bifurcation diagram	17
2.3	Flow conditions	44
2.4	Lift coefficient predictions at $C_j = 0.12$	44
2.5	Parameters used in the simulation. C_a is the axial chord and C is the chord of the airfoil with $C_a = 0.546C$	47

LIST OF FIGURES

2.1	Bifurcation diagram for homogeneous shear flows	10
2.2	Bifurcation surface: Branch 1 solution. Bright region shows imaginary solution which is not physical	11
2.3	Bifurcation diagram in homogenous shear flow	15
2.4	Testing the implementation of the curvature term	21
2.5	Comparison of mean velocity profiles at different rotation numbers	24
2.6	Rotating channel flow: Effect of rotation on bulk velocity and friction velocity	25
2.7	Skin friction plotted along the curved walls	28
2.8	Variation of rotation/curvature correction factors inside the boundary layer	29
2.9	Hydrocyclone: Axial velocity profiles at two different stations indicated on the left	30
2.10	Flow configuration of serpentine channel	32
2.11	Serpentine Channel, stationary: Comparison of mean velocity profiles with Laskowski and Durbin (2007) data. For the legend, see Fig. 2.13	32
2.12	Backward-facing step, non-rotating case	33
2.13	Backward-facing step, $Ro=0.05$: Comparison of skin friction coefficient	34
2.14	Comparison of Mean velocity profiles at $Ro=0.05$	34

2.15	Backward-facing step, $Ro=0.2$: Comparison of skin friction coefficient at $Ro=0.2$. For the legend, see Fig. 2.13	34
2.16	Comparison of Mean velocity profiles at $Ro = 0.2$	34
2.17	Reattachment length plotted as a function of rotation number. For X_1 and X_2 , see Fig. 2.12	35
2.18	Stream traces showing the combined effect of rotation and curvature. The waviness in the streamtraces is because the flow is laminar in that region and the use of turbulence model may not be appropriate.	37
2.19	Stream traces at different rotation numbers	39
2.20	Inflow mean velocity profile. Symbols: Experimental data of Cheah et al. (1996); Solid line: Computed	39
2.21	Mean velocity profiles at $Ro = 0.0$. For station numbers, see Fig.2.19	40
2.22	Mean velocity profiles at $Ro = 0.2$. For station numbers, see Fig.2.19	41
2.23	Mean velocity profiles at $Ro = -0.2$. For station numbers, see Fig.2.19	42
2.24	Turbulent shear stress profiles downstream of the bend. For station numbers, see Fig.2.19	43
2.25	Lift enhancement by blowing a jet over the trailing edge: $L'_2 > L'_1$	44
2.26	Case: $C_j = 0.12$, Stream traces over the Coanda surface	45
2.27	Pressure coefficient over the airfoil surface	45
2.28	Tip leakage vortex: Flow configuration and grid topology	47
2.29	Evolution of the tip leakage vortex: Isosurfaces of the vortex core located using Q -criterion ($ \Omega ^2 - S ^2 = +50$)	48

2.30	Eddy viscosity contours showing the effect of streamline curvature at $X/C_a = 1.366$	48
2.31	Velocity contours	49
2.32	TKE contours at $X/C_a = 1.366$	49
2.33	Velocity contours	50
2.34	TKE contours at $X/C_a = 2.062$	50
2.35	Velocity contours	51
2.36	TKE contours at $X/C_a = 2.831$	51
3.1	Flow chart of inflow turbulence generation algorithms	60
3.2	Initialization for flat plate boundary layer simulation	61
3.3	Time development of flow variables	62
3.4	Flat plate boundary layer: one-point statistics	62
3.5	Flat plate boundary layer: velocity contours	63
3.6	Flat plate boundary layer: Skin friction variation	63
3.7	Flow through plane channel: Instantaneous velocity contours	65
3.8	Flow through plane channel	65
3.9	Channel flow: Skin friction variation with different outflow bound- ary conditions	66
3.10	Flow through annulus: Instantaneous velocity contours	67
3.11	Smith's chart: Turbine efficiency curves	67
3.12	Current trends in the turbofan engines	68
3.13	Flow configuration of the turbine transition duct	69
3.14	Flow through transition duct without struts	70
3.15	Flow through transition duct with struts	70

ACKNOWLEDGEMENTS

My sincere thanks to Prof. Paul A. Durbin for his guidance, patience and support throughout this research. His insights and words of encouragement have often inspired me. His passion, innovative thinking and scientific rigor have left indelible impressions on me.

I would like to thank Prof. Alric Rothmayer, Prof. Thomas J. Rudolphi, Prof. Shankar Subramaniam and Prof. Song-Charng Kong for kindly serving on the graduate committee. Special thanks to Prof. Rudolphi for being my Preparing Future Faculty mentor.

Thanks to all my friends whose presence made my stay at Ames much more enjoyable. I cannot thank enough the support of my parents and sister without which this journey would not have been possible.

This research is partially funded by NSF-GOALI program.

ABSTRACT

In the first part of this work, two different approaches to incorporate the effects of rotation and curvature in scalar eddy viscosity models have been explored. One is the “Modified coefficients approach” - to parameterize the model coefficients such that the growth rate of turbulent kinetic energy is suppressed or enhanced. The other is the “Bifurcation approach” - to parameterize eddy-viscosity coefficient such that the equilibrium solution bifurcates from healthy to decaying solution branches. Simple, yet, predictive models in each of these two approaches are proposed and validated on some benchmark test cases characterized by profound effects of system rotation and/or streamline curvature. The results obtained with both the models are encouraging. Application of the models to some practically relevant flow configurations is also discussed.

In the second part, a computational framework is developed with recycling and rescaling method of inflow generation to perform eddy simulation of turbomachinery flows. A systematic validation is carried out on a spatially developing boundary layer on flat plate, flow through a channel and an annulus. Then, large eddy simulation of turbine transition duct is performed to demonstrate the effectiveness of this methodology.

CHAPTER 1. GENERAL INTRODUCTION

1.1 Background

The physics of incompressible turbulent fluid flows is governed by the Navier-Stokes and continuity equations. Due to the complexity of the description of these flows, it is usual to invoke a statistical theory. Statistics, like average velocity, or its variance are directly related to the skin friction, pressure coefficient that are of paramount importance to the engineering designers. But, the exact equations to these statistics do not exist. The equations for the statistics of turbulent flow are fewer than the number of unknowns and hence they do not form a closed set. The purpose of turbulence closure modeling is to use mathematical models and physical concepts to represent the effect of the unknowns in terms of the known parameters. This is called Reynolds averaged Navier-Stokes (RANS) approach.

The alternative to the RANS modeling is to solve the full three-dimensional, time-dependent Navier-Stokes equations to obtain instantaneous flow field and then perform averaging to get the statistics. This approach is called direct numerical simulations (DNS). But, DNS is quite demanding in terms of computational resources as one should use a sufficiently large number of grid points to resolve the entire spectrum of scales. Another approach is to resolve only the large, energy containing scales and model the effects of small scales. The vast computational cost of representing the small-scales can be avoided in this approach. This is called large eddy simulation (LES). Challenges such as: near-wall modeling, computational cost for practically high Reynolds numbers have

limited LES only to a few applications. More recently, turbulence literature has seen a proliferation of hybrid RANS-LES methodologies that claim to combine the advantages of RANS and LES approaches. Lack of a comprehensive theory is one reason for the proliferation of such methods. In this category, detached eddy simulation (DES) and its variants have been particularly successful for massively separated flows and making their way into the engineering analysis (Spalart, 2009).

The particular focus of this dissertation is on improving the widely used scalar RANS models for a class of flows in which frame rotation and streamline curvature can have a profound influence on the turbulence. The following principles are, in general, used as a guideline for developing mathematical models for turbulence closure problem (Durbin and Petttersson-Reif, 2010):

- Dimensional consistency
- Coordinate system independence
- Galilean invariance
- Realizability

In rotating and curved flows, formulating models that do not violate the above principles is particularly challenging and makes it an exciting research problem. Historically, the mathematical models are developed based on a combination of the following:

- Physical intuition
- Systematic theoretical guidelines
- Experimental databases, correlations
- High-fidelity databases from DNS/LES

In the first part of this work, improvements to the widely used scalar turbulence closures are proposed to predict the effects of rotation and curvature. Equilibrium analysis is used as a theoretical tool in guiding the model development supplemented by the experimental as well as DNS/LES data. In the second part, a framework to generate inflow turbulence is developed within OpenFOAM and tested for its effectiveness to perform LES of complex turbomachinery flows. The objective of this work is to generate a high-fidelity database to help guide the model development.

1.2 Original contributions of this dissertation

The original contributions of this dissertation that have been published, unpublished or prepared for submission are:

- Arolla, S.K., Durbin, P.A., Modeling rotation and curvature effects within scalar eddy viscosity model framework, published in *International Journal of Heat and Fluid Flow*.
- Arolla, S.K., Durbin, P.A., On the numerical implementation of a rotation/curvature correction to turbulence models in a finite volume CFD code, in preparation for *Progress in Computational Fluid Dynamics Journal*.
- Arolla, S.K., Durbin, P.A., Generating inflow turbulence for eddy simulation of turbomachinery flows, unpublished.

The first two articles form chapter 2 and the last article chapter 3 of this thesis. The general conclusions derived from this work are summarized in chapter 4.

CHAPTER 2. MODELING ROTATION AND CURVATURE EFFECTS WITHIN SCALAR EDDY VISCOSITY MODEL FRAMEWORK

2.1 Abstract

Two approaches to incorporate the effects of rotation and curvature in scalar eddy viscosity models are explored. One is the “Modified coefficients approach” - to parameterize the model coefficients such that the growth rate of turbulent kinetic energy is suppressed or enhanced. The other is the “Bifurcation approach” - to parameterize the eddy viscosity coefficient such that the equilibrium solution bifurcates from healthy to decaying solution branches. Simple, yet, predictive models in each of these two approaches are proposed and validated on some benchmark test cases characterized by profound effects of system rotation and/or streamline curvature. The results obtained with both the models are encouraging.

2.2 Introduction

Scalar turbulence closure models are the workhorses of industrial CFD. But, their native formulation is insensitive to rotation and curvature. Second moment closures (SMC) can account for these effects in a systematic manner because of the presence of exact production terms containing mean flow gradients and system rotation. They also contain the convective transport of the second moments and hence provide an accu-

rate means for predicting the curved flows. Explicit Algebraic Reynolds Stress Models (EARSM) also retain the exact production terms, but are not frame invariant. Invariant methods have been proposed by Girimaji (1997) using an acceleration based coordinate system and by Gatski and Jongen (2000) using a strain rate based coordinate system following the ideas of Spalart and Shur (1997). But, the SMCs and the EARSMs are still not tractable in complex industrial applications due to excessive computational cost and numerical stiffness. This is the motivation to incorporate rotation/curvature effects into the scalar, eddy viscosity framework.

Methods to sensitize scalar turbulence closure models to rotation and curvature can be categorized into the “Modified coefficients approach” and the “Bifurcation approach”. A review of the machinery used in these approaches can be found in Durbin (2011).

The modified coefficients approach dates back to 1980. Howard et al. (1980) modified turbulence length scale by adding rotation dependent terms to the dissipation rate equation. Several others also have introduced ad-hoc rotation/curvature dependent terms into the ε transport equation (Cazalbou et al., 2005). Hellsten (1998) extended the work of Khodak and Hirsch (1996) by introducing parametric dependency into the destruction term of the specific dissipation rate equation. Spalart and Shur (1997) introduced a correction to the production term in a transport equation for eddy viscosity. They proposed a unified measure for rotation and curvature in terms of the material derivative of the strain rate tensor, making the model frame independent and Galilean invariant. More recently, Smirnov and Menter (2009) applied the Spalart-Shur correction to the SST variant of $k - \omega$ by correcting the production terms in both the TKE and the ω transport equations. A criticism of a model which corrects the production term in the TKE equation without a corresponding correction of the eddy viscosity in the momentum equation is that it violates energy conservation: energy extracted from the mean flow by the turbulence is not in balance with the production of turbulent kinetic energy.

Pettersson-Reif et al. (1999) proposed a novel approach to sensitize the scalar turbu-

lence models to rotational effects. Bifurcation analysis of SMCs in rotating homogeneous shear flow forms the basis for this work. The model is formulated such that the equilibrium solution bifurcates from healthy to decaying solution branches. The original method was proposed in conjunction with the $v^2 - f$ model. In principle, it can be used with any scalar turbulence model, but prior to the present paper, that has not been pursued. Duraisamy and Iaccarino (2005) have extended this for curved flows and tested it on a tip vortex. Dhakal and Walters (2011) follow a similar approach, but they introduce an additional equation to tackle numerical convergence issues.

In this work, we follow the approach proposed by Pettersson-Reif et al. (1999) with an objective to simplify the functional form of the model while retaining the predictive capability. We perform the analysis of the proposed model for its bifurcation behavior in homogeneous curved shear flow and compare the salient points on the bifurcation diagram with that using the linearized SSG model. Based on the understanding gained from the bifurcation approach, we also propose a simple model to parameterize the production term in the ω transport equation. The two new models are tested on several cases in which rotation and curvature are known to have profound influence.

Since the modeling framework proposed in this work unifies rotation and curvature, we use the terminology “rotation correction” and “curvature correction” interchangeably throughout this paper.

2.3 Analysis of the Second Moment Closures

2.3.1 Analogy between rotation and curvature

The evolution equation for the Reynolds stress anisotropy tensor in a rotating frame of reference is given by (Durbin and Pettersson-Reif, 2010):

$$\begin{aligned} \frac{k}{\varepsilon} d_t a_{ij} = & (1 - C_1) a_{ij} - a_{ij} \mathcal{P}_{\mathcal{R}} - (4/3 - C_s) S_{ij}^* \\ & \underbrace{- a_{ik} S_{kj}^* - a_{jk} S_{ki}^* + 2/3 \delta_{ij} a_{kl} S_{lk}^* - a_{ik} \Omega_{kj}^* - a_{jk} \Omega_{ki}^*}_{\mathbf{\Pi}_{\text{rotation/curvature}}} \end{aligned} \quad (2.1)$$

where

$$\begin{aligned} a_{ij} &= (1 - C_2 - C_3) [\overline{u_i u_j} / k - (2/3) \delta_{ij}] \\ S_{ij}^* &= [(1 - C_2 - C_3) S_{ij}] \frac{k}{\varepsilon} \\ \Omega_{ij}^* &= [(1 - C_2 + C_3) \Omega_{ij}^A + \epsilon_{ijl} \Omega_l^F] \frac{k}{\varepsilon} \end{aligned} \quad (2.2)$$

and the rate of production due to mean flow gradients and rotation/curvature is

$$\begin{aligned} \mathcal{P}_{ij} &= -\overline{u_i u_k} (S_{kj} + \Omega_{kj}^A) - \overline{u_j u_k} (S_{ki} + \Omega_{ki}^A) \\ \mathcal{P}_{\mathcal{R}} &= \mathcal{P} / \varepsilon; \quad \mathcal{P} = \mathcal{P}_{kk} / 2 \end{aligned} \quad (2.3)$$

with the strain rate tensor and the absolute rotation tensor defined as

$$\begin{aligned} S_{ij} &\equiv 1/2 (\partial_i U_j + \partial_j U_i) \\ \Omega_{ij}^A &\equiv 1/2 (\partial_i U_j - \partial_j U_i) + \epsilon_{ijk} \Omega_k^F \end{aligned} \quad (2.4)$$

where Ω_k^F is the angular frame velocity about x_k -axis. This will be denoted by Ω^F .

The constants for the linearized SSG model are: $C_2 = 0.4125$, $C_3 = 0.2125$, $C_s = 0.1844$ and $C_1 = 3.4$. The standard $k - \varepsilon$ model equations are used to complete the closure at this level.

In parallel shear flow subjected to orthogonal mode rotation, the non-dimensional strain rate tensor is given by

$$S_{ij}^* = \frac{1}{2} C_{S^*} \frac{Sk}{\varepsilon} \begin{pmatrix} 0 & 1 & 0 \\ 1 & 0 & 0 \\ 0 & 0 & 0 \end{pmatrix}$$

and the non-dimensional rotation rate tensor is given by

$$\Omega_{ij}^* = \frac{1}{2} C_{\Omega^*} \frac{Sk}{\varepsilon} \left(1 - 2C_r \frac{\Omega^F}{\mathcal{S}} \right) \begin{pmatrix} 0 & -1 & 0 \\ 1 & 0 & 0 \\ 0 & 0 & 0 \end{pmatrix}$$

where $C_r = (2 - C_2 + C_3)/(1 - C_2 + C_3) = 2.25$, $C_{S^*} = (1 - C_2 - C_3) = 0.375$ and $C_{\Omega^*} = (1 - C_2 + C_3) = 0.8$ for the pressure-strain model considered.

It can be observed from equation 2.1 that frame rotation enters the evolution equation only through the last two of the underbraced terms. They contain contributions from both flow rotation and coordinate frame rotation. By substituting non-dimensional strain rate and rotation rate, the rate of production of the Reynolds shear stress anisotropy becomes:

$$\Pi_{12(\text{rotation})} = \frac{Sk}{\varepsilon} \left[[a_{11}C_3 - a_{22}(1 - C_2)] - \frac{\Omega^F}{\mathcal{S}}(2 - C_2 + C_3)(a_{11} - a_{22}) \right] \quad (2.5)$$

Consider a case with $\mathcal{S} > 0$ and a positive imposed rotation, $\Omega^F > 0$. Usually, $a_{11} > a_{22}$ in parallel shear flow. Hence, equation 2.5 shows that frame rotation decreases the rate of production of the Reynolds shear stress anisotropy. This means that the magnitude of shear stress production is increased, since \overline{uv} is negative in parallel shear flows. Negative rotation has the opposite effect.

In curved homogeneous shear flow, the non-dimensional strain rate tensor is given by

$$S_{ij}^* = \frac{1}{2} C_{S^*} \frac{Sk}{\varepsilon} (1 - \xi) \begin{pmatrix} 0 & 1 & 0 \\ 1 & 0 & 0 \\ 0 & 0 & 0 \end{pmatrix}$$

The non-dimensional rotation rate tensor is

$$\Omega_{ij}^* = \frac{1}{2} C_{\Omega^*} \frac{\mathcal{S}k}{\varepsilon} [1 + \xi + 2(C_r - 1)\xi] \begin{pmatrix} 0 & -1 & 0 \\ 1 & 0 & 0 \\ 0 & 0 & 0 \end{pmatrix}$$

By substituting non-dimensional strain rate and rotation rate tensor components into the underbraced terms of equation 2.1, the rate of production of the Reynolds shear stress anisotropy becomes:

$$\Pi_{12(\text{curvature})} = \frac{\mathcal{S}k}{\varepsilon} \left[[a_{11}C_3 - a_{22}(1 - C_2)][1 - \xi] + \xi(2 - C_2 + C_3)(a_{11} - a_{22}) \right] \quad (2.6)$$

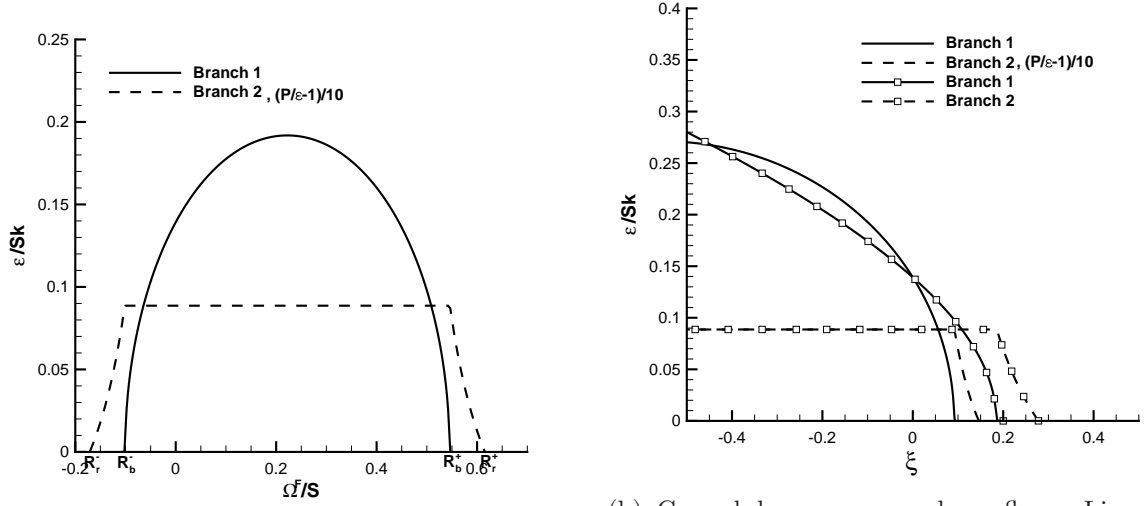
Which can be compared to equation 2.5. The analogy between rotation and curvature is through the second term in equation 2.6. In practice, this is dominant over the curvature contribution through the first term. For $\mathcal{S} > 0$ and $\xi > 0$, curvature results in increased rate of production of the Reynolds shear stress anisotropy. The magnitude of shear stress production, however, is decreased because \overline{uv} is negative in parallel shear flows. $\xi < 0$ results in increased magnitude of shear stress production. Hence, curvature is analogous to rotation in that it can either suppress or amplify production of turbulent shear stress. It can be observed that ξ has the same role as $-\Omega^F/\mathcal{S}$ in rotating flows.

2.3.2 Bifurcation analysis: Combined effects of rotation and curvature

We use the framework developed in Durbin and Petttersson-Reif (2010) for the bifurcation analysis of SMCs and extend it to the combined effects of rotation and curvature making use of the analogy between rotation and curvature developed in section 2.3.1.

An explicit solution is sought for equation 2.1 with $d_t a_{ij} = 0$ resulting in the following relation for $\varepsilon/\mathcal{S}k$ vs. Ω^F/\mathcal{S} , termed the branch 1 solution:

$$\frac{(1/4)(\varepsilon/\mathcal{S}k)_{\infty}^2}{g^2(1 - \xi)^2(1 - C_2 - C_3)^2} = \frac{2}{3} + \frac{(4/3 - C_s)}{(1 - C_2 - C_3)^2 g \mathcal{P}_{\mathcal{R}}} - 2 \frac{(1 - C_2 + C_3)^2}{(1 - C_2 - C_3)^2} \mathcal{R}^2 \quad (2.7)$$



(a) Rotating homogeneous shear flow

(b) Curved homogeneous shear flow: Lines with symbols are for the case with the convective transport neglected

Figure 2.1 Bifurcation diagram for homogeneous shear flows

where $g = 1/(C_1 - 1 + \mathcal{P}_{\mathcal{R}})$.

On the branch 2, $\varepsilon/k = 0$. Setting this and rearranging equation 2.7 gives

$$(4/3 - C_s) \frac{C_1 - 1 + \mathcal{P}_{\mathcal{R}}}{\mathcal{P}_{\mathcal{R}}} = 2(1 - C_2 + C_3)^2 \mathcal{R}^2 - \frac{2}{3}(1 - C_2 - C_3)^2 \quad (2.8)$$

which gives $\mathcal{P}_{\mathcal{R}}$ vs. \mathcal{R} on branch 2. The definition of \mathcal{R} has been generalized for the case with both rotation and curvature as:

$$\mathcal{R}^2 \equiv \left(\frac{\Omega(1 + \xi)}{\mathcal{S}(1 - \xi)} + 2 \frac{(2 - C_2 + C_3)\Omega^F}{(1 - C_2 + C_3)\mathcal{S}(1 - \xi)} - 2 \frac{\xi}{(1 - C_2 + C_3)(1 - \xi)} \right)^2 \quad (2.9)$$

with $\Omega = -\partial_y U$ and $\mathcal{S} = \partial_y U$ in homogeneous shear flow.

The bifurcation diagrams plotted in Fig. 2.1 for rotating homogeneous shear flow and curved homogeneous shear flow are special cases in equation 2.9 with $\xi = 0$ and $\Omega^F/\mathcal{S} = 0$ respectively. In Fig. 2.2, we compare the effect of neglecting the convective transport (corresponds to the last term in equation 2.9), while taking the equilibrium approximation. The plot indicates that turbulence stabilization occurs much earlier when

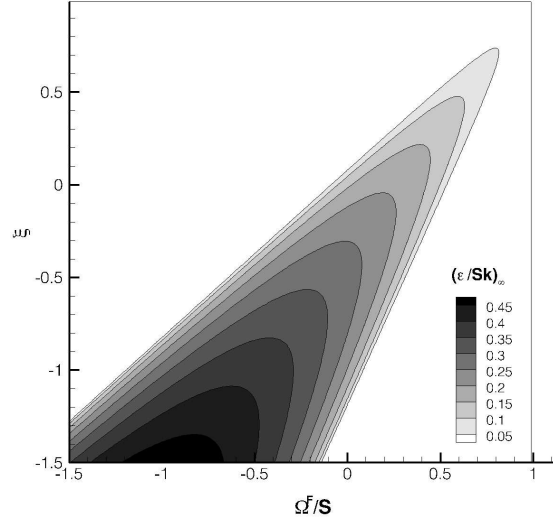


Figure 2.2 Bifurcation surface: Branch 1 solution. Bright region shows imaginary solution which is not physical

the convective transport term is included, underscoring the importance of this term. The bifurcation surface for the combined effects of rotation and curvature is plotted in Fig. 2.2. It can be observed that when $\Omega^F/\mathcal{S} > -0.15$, there is a second ξ -bifurcation point. It means that the linearized SSG model predicts stabilization even for concave curvatures in non-rotating flows which is unphysical.

2.4 Scalar eddy viscosity model framework

Stated briefly, the SST model is of the form

$$\frac{\partial k}{\partial t} + u_j \frac{\partial k}{\partial x_j} = \mathcal{P} - \varepsilon + \frac{\partial}{\partial x_j} \left[\left(\nu + \frac{\nu_T}{\sigma_k} \right) \frac{\partial k}{\partial x_j} \right] \quad (2.10)$$

where $\varepsilon = \beta^* k \omega$ and $\mathcal{P} = \nu_t \mathcal{S}^2$.

$$\frac{\partial \omega}{\partial t} + u_j \frac{\partial \omega}{\partial x_j} = \frac{\gamma}{\nu_T} \mathcal{P} - D_\omega + \frac{\partial}{\partial x_j} \left[\left(\nu + \frac{\nu_T}{\sigma_\omega} \right) \frac{\partial \omega}{\partial x_j} \right] + CD_\omega \quad (2.11)$$

where $D_\omega = \beta \omega^2$ and CD_ω is the cross-diffusion term. The eddy viscosity, with no accounting for curvature effects, is $\nu_T = C_\mu k/\omega$ with $C_\mu = 1.0$.

2.4.1 Bifurcation approach

In homogeneous shear flow, the turbulent kinetic energy and dissipation rate evolve as

$$\frac{Dk}{Dt} = \mathcal{P} - \varepsilon; \quad \frac{D\varepsilon}{Dt} = \frac{C_{\varepsilon 1}\mathcal{P} - C_{\varepsilon 2}\varepsilon}{T} \quad (2.12)$$

Combining these equations results in the following evolution equation for the timescale ratio

$$\frac{D}{D(\mathcal{S}t)} \left(\frac{\varepsilon}{\mathcal{S}k} \right) = \left(\frac{\varepsilon}{\mathcal{S}k} \right)^2 \left[(C_{\varepsilon 1} - 1)\mathcal{P}_{\mathcal{R}} - (C_{\varepsilon 2} - 1) \right] \quad (2.13)$$

where $\mathcal{P}_{\mathcal{R}} = \mathcal{P}/\varepsilon$.

This equation admits two equilibria by setting the left hand side to zero (Speziale and MacGiollaMhuiris, 1989). They are:

$$\mathcal{P}_{\mathcal{R}} = (C_{\varepsilon 2} - 1)/(C_{\varepsilon 1} - 1); \quad \left(\frac{\varepsilon}{\mathcal{S}k} \right)_{\infty} = 0 \quad (2.14)$$

The point at which both these equilibrium solutions coexist is the bifurcation point. Durbin and Petttersson-Reif (1999) noted that SMC model bifurcation is not immediately a stabilizing bifurcation. Turbulence stabilization occurs past the bifurcation point at the so-called restabilization point where the ratio of turbulence production to dissipation rate is equal to 1.

The idea in this approach is to introduce a functional dependence into the eddy viscosity coefficient (C_{μ}) such that the model bifurcates. In rotating and convexly curved flows, the turbulence production decreases. If the rate of rotation or the convex curvature is strong enough, turbulence can no longer be sustained resulting in relaminarization. We use a functional dependency on C_{μ} to create this effect directly.

2.4.1.1 Petttersson-Reif et al. extended to SST $k - \omega$

Petttersson-Reif et al. (1999) introduce their model into the $v^2 - f$ turbulence model. We extend this to the $k - \omega$ model as $\nu_T = C_{\mu}^*k/\omega$. In Petttersson-Reif et al., the

functional form for the rotation correction is given by:

$$C_\mu^* = \frac{1 + \alpha_2|\eta_3| + \alpha_3\eta_3}{1 + \alpha_4|\eta_3|} \left(\sqrt{\frac{1 + \alpha_5\eta_1}{1 + \alpha_5\eta_2}} + \alpha_1\sqrt{\eta_2}\sqrt{|\eta_3| - \eta_3} \right)^{-1} \quad (2.15)$$

where $\eta_1 \equiv S_{ij}^*S_{ij}^*$; $\eta_2 \equiv \Omega_{ij}^*\Omega_{ij}^*$ and $\eta_3 \equiv \eta_1 - \eta_2$. The model constants are: $\alpha_1 = 0.055$, $\alpha_2 = 0.5$, $\alpha_3 = 0.25$, $\alpha_4 = 0.2$, $\alpha_5 = 0.025$. Unlike Petttersson-Reif et al., we do not use damping functions. Also, C_μ^* is limited to a maximum value of 2.5.

2.4.1.2 Proposed new model

The functional form proposed by Petttersson-Reif et al. uses the bifurcation diagram of SMCs as a tool in guiding the model development. But, there is no evidence in the literature that suggests the models should behave exactly in the same way as SMCs as the parameter Ω^F/\mathcal{S} is varied. So, our idea in this work is to follow the same approach but enforce only the bifurcation and restabilization points to be close to SMCs. We do not enforce the SMCs behavior for the entire range of Ω^F/\mathcal{S} . The following constraints are imposed on the functional form for a well-behaved model. The model should:

- Retain the original form in the absence of curvature or rotation ($C_\mu^* = C_\mu$).
- Bifurcate between only two possible stable non-rotating solutions: $(\varepsilon/\mathcal{S}k)_\infty = 0.208$; $(\varepsilon/\mathcal{S}k)_\infty = 0$.
- Yield restabilization close to $\Omega^F/\mathcal{S} = 0$ & 0.5 in rotating homogeneous shear flow.
- Yield a maximum value of $(\varepsilon/\mathcal{S}k)$ close to $\Omega^F/\mathcal{S} = 0.25$.
- Behave as $C_\mu \approx \eta_1^{-1}$ as $\eta_1 \rightarrow \infty$ so that $\lim_{\eta_1 \rightarrow \infty} C_\mu^*\eta_1$ is finite.
- Behave as $C_\mu^* \approx 1/\sqrt{\eta_1}$ when $\eta_1 \gg \eta_2$.

Several functional forms have been tried and we selected the following:

$$C_\mu^* = C_\mu \left(\alpha_1(|\eta_3| - \eta_3) + \sqrt{1 - \min(\alpha_2\eta_3, 0.99)} \right)^{-1}$$

To evaluate the model coefficients, we insert C_μ^* in the moving equilibrium solution: on branch 1,

$$\mathcal{P}/\varepsilon = (C_{\varepsilon 2} - 1)/(C_{\varepsilon 1} - 1) \quad (2.16)$$

For the $k - \varepsilon$ model, $\mathcal{P} = 2\nu_t|S|^2 \equiv \nu_t\mathcal{S}^2$ where ν_t is the eddy viscosity, $C_\mu^*k^2/\varepsilon$. Substitution into equation 2.16 gives

$$\left(\frac{\varepsilon}{\mathcal{S}k}\right)^2 = C_\mu^*(C_{\varepsilon 1} - 1)/(C_{\varepsilon 2} - 1) \quad (2.17)$$

In parallel shear flow subjected to orthogonal mode rotation, the non-dimensional strain rate tensor is given by

$$S_{ij}^* = \frac{1}{2} \frac{\mathcal{S}k}{\varepsilon} \begin{pmatrix} 0 & 1 & 0 \\ 1 & 0 & 0 \\ 0 & 0 & 0 \end{pmatrix}$$

and the non-dimensional rotation rate tensor is given by

$$\Omega_{ij}^* = \frac{1}{2} \frac{\mathcal{S}k}{\varepsilon} \left(1 - 2C_r \frac{\Omega^F}{\mathcal{S}}\right) \begin{pmatrix} 0 & -1 & 0 \\ 1 & 0 & 0 \\ 0 & 0 & 0 \end{pmatrix}$$

The dimensionless velocity gradient invariants are

$$\begin{aligned} \eta_1 &\equiv S_{ij}^* S_{ij}^* = \frac{1}{2} (\mathcal{S}k/\varepsilon)^2 \\ \eta_2 &\equiv \Omega_{ij}^* \Omega_{ij}^* = -\Omega_{ij}^* \Omega_{ji}^* = \frac{1}{2} (\mathcal{S}k/\varepsilon)^2 \left(1 - 2C_r \frac{\Omega^F}{\mathcal{S}}\right)^2 \\ \eta_3 &\equiv \eta_1 - \eta_2; \quad \mathfrak{R}^2 \equiv \frac{\eta_2}{\eta_1} = \left(1 - 2C_r \frac{\Omega^F}{\mathcal{S}}\right)^2 \end{aligned} \quad (2.18)$$

$C_r = 2.0$ was found to give best agreement with the data for the test cases considered in this study.

Model	$(\Omega^F/\mathcal{S})_{bifurcation}$	$(\Omega^F/\mathcal{S})_{restabilization}$
Petterson-Reif et al. (with $C_r = 2.25$)	(+0.522, -0.075)	(+0.6065, -0.162)
New model	(+0.597, -0.097)	(+0.678, -0.178)
linearized SSG	(+0.550, -0.1)	(+0.620, -0.17)

Table 2.1 Comparison of salient points on the bifurcation diagram. \mathcal{S} is shear rate

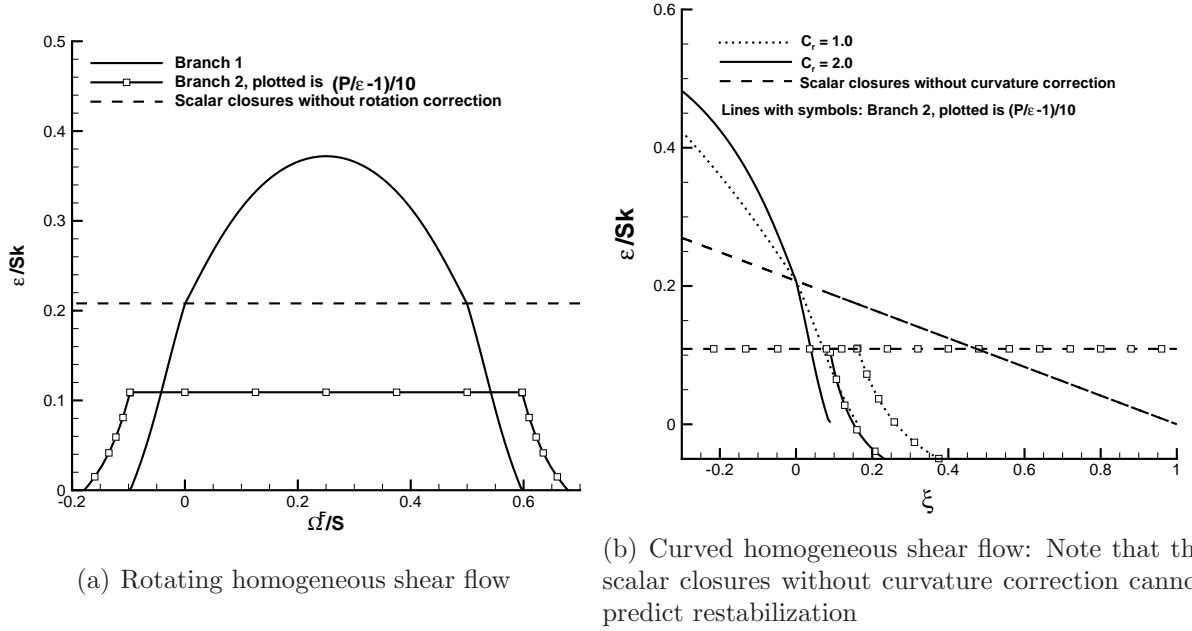


Figure 2.3 Bifurcation diagram in homogenous shear flow

After substituting equation 2.16, equation 2.17 becomes

$$\left[\alpha_1 \left(|1 - \mathfrak{R}^2| - (1 - \mathfrak{R}^2) \right) - 0.086086 \right]^2 = \frac{1}{\eta_1^2} - \frac{1}{\eta_1^2} \min [\alpha_2 \eta_1 (1 - \mathfrak{R}^2), 0.99]$$

When plotted as $\varepsilon/\mathcal{S}k$ vs. Ω^F/\mathcal{S} , this is branch 1 of the bifurcation diagram as shown in Fig. 2.3.

On branch 2, the solution is trivial $\varepsilon/\mathcal{S}k \equiv 1/\sqrt{2\eta_1} = 0$. In Fig. 2.3, the points where $\mathcal{P}_{\mathcal{R}} \equiv \mathcal{P}/\varepsilon$ crosses unity on the Y-axis give the restabilization points. The analysis starts with $\mathcal{P}_{\mathcal{R}}$, given by:

$$\mathcal{P}_{\mathcal{R}} = C_{\mu}^* (\mathcal{S}k/\varepsilon)^2$$

Substituting for C_μ^* and taking the limit $\eta_1 \rightarrow \infty$,

$$\mathcal{P}_R = \frac{2C_\mu}{\alpha_1 \left[|1 - \Re^2| - (1 - \Re^2) \right]} \quad (2.19)$$

which is plotted as branch 2 on the bifurcation diagram (see Fig. 2.3). The model coefficients are tuned such that the bifurcation and restabilization points predicted by the proposed model are close to the SMCs. We selected $\alpha_1 = 0.04645$ and $\alpha_2 = 0.25$ and C_μ^* is limited to a maximum value of 2.5. From table 2.1, it can be concluded that the bifurcation and restabilization points predicted by both Petterson-Reif et al. and the proposed new model are in close agreement with the linearized SSG model (see 2.3.2 for bifurcation analysis of the linearized SSG model).

Now, let us consider curved homogeneous shear flow. It is a homogeneous idealization of a flow with circular streamlines (Holloway and Tavoularis, 1989). Homogeneity in a flow confined between inner and outer cylindrical walls can be sought in the limit of large radii and by assuming that the distance between the two walls is far greater than the turbulence length scales. Curved homogeneous shear flow is characterized by shear rate and curvature factor given by

$$\mathcal{S} = \frac{\partial U}{\partial r}, \quad \xi = \left(\frac{U_c}{R_c} \right) / \mathcal{S} \quad (2.20)$$

where the tangential velocity, $U = U_c + \mathcal{S}r$ with \mathcal{S} being constants in homogeneous shear flow; R_c is the radius of curvature and r is the radial coordinate measured from the center of the curvature. $\xi > 0$ corresponds to convex curvature which is stabilizing, $\xi < 0$ corresponds to concave curvature which is destabilizing.

The non-dimensional strain rate tensor for this case is obtained by transforming to the streamline coordinate system and is given by

$$S_{ij}^* = \frac{1}{2} \frac{\mathcal{S}k}{\varepsilon} (1 - \xi) \begin{pmatrix} 0 & 1 & 0 \\ 1 & 0 & 0 \\ 0 & 0 & 0 \end{pmatrix}$$

Model	$\xi_{bifurcation}$	$\xi_{restabilization}$
$C_r = 1.0$	0.162	0.263
$C_r = 2.0$	0.089	0.1515
linearized SSG	0.1	0.15

Table 2.2 Salient points on the bifurcation diagram

The non-dimensional rotation rate tensor is given by

$$\Omega_{ij}^* = \frac{1}{2} \frac{\mathcal{S}k}{\varepsilon} [1 + \xi + 2(C_r - 1)\xi] \begin{pmatrix} 0 & -1 & 0 \\ 1 & 0 & 0 \\ 0 & 0 & 0 \end{pmatrix}$$

The dimensionless velocity gradient invariants are

$$\begin{aligned} \eta_1 &\equiv S_{ij}^* S_{ij}^* = \frac{1}{2} (\mathcal{S}k/\varepsilon)^2 (1 - \xi)^2 \\ \eta_2 &\equiv \Omega_{ij}^* \Omega_{ij}^* = -\Omega_{ij}^* \Omega_{ji}^* = \frac{1}{2} (\mathcal{S}k/\varepsilon)^2 [1 + \xi + 2(C_r - 1)\xi]^2 \\ \eta_3 &\equiv \eta_1 - \eta_2; \quad \mathfrak{R}^2 \equiv \frac{\eta_2}{\eta_1} \end{aligned} \tag{2.21}$$

As \mathfrak{R} is now a function of ξ alone, the solution can be plotted as $\mathcal{P}_{\mathcal{R}}$ vs. ξ as shown in Fig. 2.3.

From Fig. 2.3, it can be observed that there is only one bifurcation point in curved homogeneous shear flow. The higher the value of C_r , the earlier the restabilization is. As shown in table 2.2, the proposed model with $C_r = 2.0$ predicts the bifurcation and restabilization points in close agreement with those predicted by the linearized SSG model (see 2.3.2).

2.4.2 Modified coefficients approach

2.4.2.1 Proposed η_3 based model

With the understanding gained from the bifurcation approach, we propose a modified coefficient model for the production term of the ω -equation. Replace the first term on

the right side of equation 2.11 by $P_\omega = \gamma F_{rc} \mathcal{S}^2$ where

$$F_{rc} = (1.0 + \alpha_1 |\eta_3| + 3\alpha_1 \eta_3) \quad (2.22)$$

In our previous work (Arolla and Durbin, 2012a), we have tried correcting the destruction term of the TKE equation. Although, it did give good results in some benchmark test cases, it can interfere with the stress limiter and blending functions defined in the base turbulence model and hence can cause troubles in complex cases.

Since F_{rc} is not bounded, we impose an upper clip at 10.0 which was sufficiently high to cause the stabilization of turbulence and a lower clip at 0.0 to avoid negative dissipation. A value of $\alpha_1 = -0.2$ was found to be optimum for the cases tested here.

2.4.2.2 *Br* based model (Hellsten; Khodak & Hirsch)

We will compare to a model of Hellsten (1998). This model is motivated by the Bradshaw number $Br = Ro(Ro + 1)$ where $Ro \equiv -2\Omega^F / \partial_y U$. Khodak and Hirsch (1996) suggest replacing frame rotation in the Bradshaw number by $|\mathbf{\Omega}^A| - |\mathbf{S}|$. Hellsten (1998) uses $D_\omega = F_4 \beta \omega^2$ for the destruction term in the ω -equation with

$$F_4 = \frac{1}{1 + C_{RC} Br} \quad (2.23)$$

where $Br = \sqrt{\frac{\eta_2}{\eta_1}} \left(\sqrt{\frac{\eta_2}{\eta_1}} - 1 \right)$. The model constants are: $C_{RC} = 3.6$ and $C_r = 1.0$.

2.4.3 Unification of rotation and curvature

Rotation and curvature are analogous. Analysis of SMCs to understand this analogy is outlined in 2.3.1. For turbulence closure modeling, rotation and curvature can be unified using Spalart-Shur tensor as discussed in Durbin (2011). The definitions of the rate of strain and rate of rotation are given by:

$$S_{ij} = \frac{1}{2}(\partial_j U_i + \partial_i U_j); \quad \Omega_{ij}^{mod} = \Omega_{ij}^A + (C_r - 1)W_{ij}^A \quad (2.24)$$

where $\Omega_{ij}^A = \Omega_{ij}^{rel} + \Omega_{ij}^F$ with $\Omega_{ij}^{rel} = \frac{1}{2}(\partial_i U_j - \partial_j U_i)$ and $\Omega_{ij}^F = -\epsilon_{ijk}\Omega_k^F$. Ω_k^F is the angular frame velocity about the x_k -axis. The Spalart-Shur tensor is defined in terms of the strain rate tensor as:

$$\boldsymbol{\Omega}^{SS} \equiv \boldsymbol{\Omega}^F - \frac{\mathbf{S} \cdot D_t \mathbf{S} - D_t \mathbf{S} \cdot \mathbf{S}}{2|\mathbf{S}|^2} \quad (2.25)$$

In 2D, $W_{ij}^A = \Omega_{ij}^{SS}$. In 3D, this is changed to $W_{jk}^A = \Omega_{jk}^F - \epsilon_{ijk}w_i$ in which

$$w_i = II_S X_{ij} (\Omega_{pq}^F \epsilon_{pqj} - \Omega_{rs}^{SS} \epsilon_{rsj})$$

$$X_{ij} = \frac{II_S^2 \delta_{ij} + 12III_S S_{ij} + 6II_S S_{ik} S_{kj}}{2II_S^3 - 12III_S^2}$$

where $II_S = S_{ij}S_{ji}$ and $III_S = S_{ij}S_{jk}S_{ki}$.

The invariants used in the models are

$$\eta_1 = S_{ij}S_{ij}T^2; \quad \eta_2 = \Omega_{ij}^{mod}\Omega_{ij}^{mod}T^2; \quad \eta_3 = \eta_1 - \eta_2$$

The coefficient C_r takes a value of 2 for the bifurcation approach and for the η_3 based model. For the Br based model, $C_r = 1$. This means that the Br based model does not use the Spalart-Shur tensor. The numerical implementation of the models is discussed elsewhere (Arolla and Durbin, 2012b).

2.5 Numerical implementation in a finite volume CFD code

The implementation of curvature corrections in a CFD code involves computing the material derivative $D_t \mathbf{S} = \partial_t \mathbf{S} + \mathbf{U} \cdot \nabla \mathbf{S}$, which contains the third order tensor $\partial_i \partial_j U_k$. We have tested two approaches for implementing $D_t \mathbf{S}$: Eulerian and Lagrangian. The following discussion is for a cell-centered finite volume code.

In the Eulerian approach, the derivative of the strain rate tensor is computed using the Green-Gauss theorem. For steady-state incompressible flows, the time derivative is zero once the solution is converged. Then

$$\nabla \cdot (\mathbf{US}) \rightarrow \frac{1}{V} \left[\sum_{k=1}^N S_{ij}^k V_n^k \sigma^k \right] \quad (2.26)$$

where N is the number of faces, k is the face index, σ^k is area of the face with index k and V is the volume of the computational cell. The face center values of the strain rate tensor, S_{ij} and face normal velocity, V_n are obtained by linear interpolation from two neighboring cells. This procedure gives second order accuracy in space. For unsteady simulations, one must add the time derivative. This requires calculation of 15 gradients each time step in a 3D simulation, given that the strain rate tensor is symmetric and the flow is incompressible. Moreover, if highly skewed cells are used, a non-orthogonal correction is required.

To avoid these issues, a Lagrangian approach is explored in this work based on a particle tracing algorithm in the physical space (Durbin, 2011). The algorithm involves the following steps:

1. Integrate $d_t \mathbf{X} = \mathbf{U}(\mathbf{X}, t)$ to find the new location of the fluid particle starting at a computational cell center $\mathbf{X}(t) = x$. We used a simple Euler explicit time integration. The time step in steady simulations is chosen such that the particle remains within the cell where it started. In unsteady computations, the physical time step can be used.

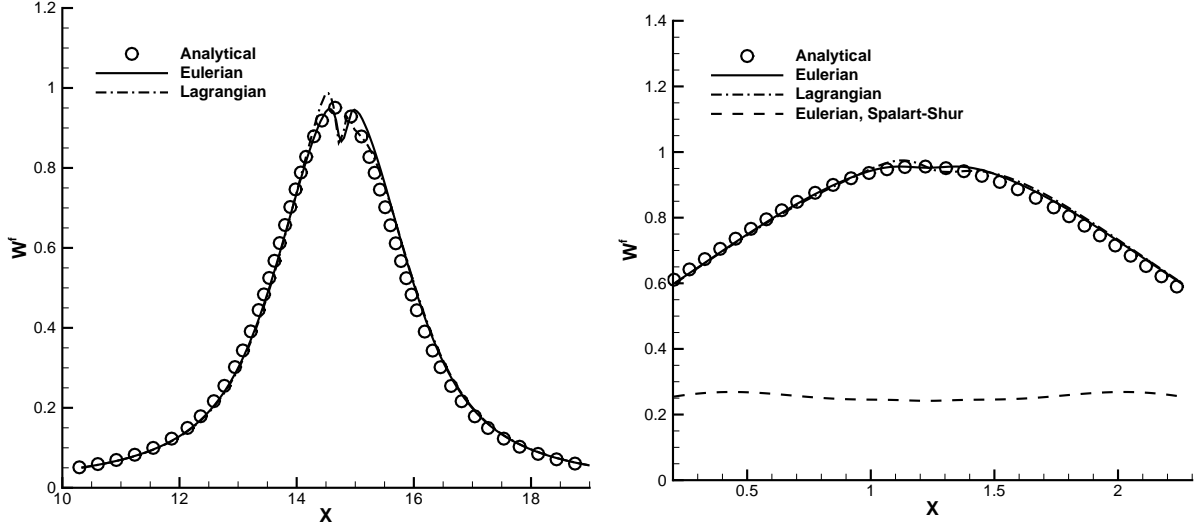
2. Interpolate the strain rate tensor and the velocity components at the new particle location. We used bilinear interpolation for 2D and trilinear interpolation for 3D. The interpolation is first order accurate and it was found to be sufficient in the examples tested.

Then, the Lagrangian derivative is evaluated as:

$$D_t \mathbf{S} \approx [\mathbf{S}(\mathbf{X}, t + \delta t) - \mathbf{S}(\mathbf{X}, t)] / \delta t \quad (2.27)$$

Once the Lagrangian derivative of the strain rate tensor is computed, the rotation rate tensor is obtained from equation 2.25.

The accuracy of the implementation is tested on two “toy problems” with analytically known streamline curvature: Lamb-Oseen vortex and Lamb-Oseen vortex with an axial flow.



(a) Lamb-Oseen vortex: U_θ/r plotted just above the vortex core
 (b) Lamb-Oseen vortex with an axial component: U_θ/r plotted just above the vortex core

Figure 2.4 Testing the implementation of the curvature term

2.5.1 Toy problem 1: Lamb-Oseen vortex

The mathematical model for the Lamb-Oseen vortex is defined in terms of angular velocity $u_\theta = rF(r)$ by (Durbin and Medic, 2007):

$$F = \frac{\Gamma}{2\pi r^2}(1 - e^{-r^2/R^2}) \quad (2.28)$$

The axial velocity is zero. Let the circulation contained within the vortex be, $\Gamma = 2\pi$ and $R = 1$. Then, the angular velocity becomes $u_\theta = \frac{1}{r}(1 - e^{-r^2})$. Note that $u_\theta \rightarrow 0$ as $r \rightarrow 0$. The streamline curvature for this case equals u_θ/r . The two approaches are compared with the analytical solution in Fig.2.4. The line plot at a location slightly away from the vortex core shows that the computed streamline curvature matches exactly with the analytical solution. This verifies the implementation and shows that both the approaches are equally accurate.

2.5.2 Toy problem 2: Lamb-Oseen vortex with an axial component

As an example for 3D flow, an axial velocity is imposed on the Lamb-Oseen vortex. The resulting velocity field has $u_\theta = \frac{1}{r}(1 - e^{-r^2})$ and $u_z = r$. We used Wallin-Johansson's extension of Spalart-Shur's idea to 3D for this case. The results plotted in Fig.2.4 also indicate that both Lagrangian and Eulerian approaches are equally accurate. We also compare the streamline curvature term predicted by the Spalart-Shur tensor and Wallin-Johansson's extension to show the difference. Our results show that the curvature is under-predicted by Spalart-Shur formula, consistent with the analysis in Wallin and Johansson (2002).

In the above examples, both the approaches of computing DS_{ij}/Dt found to be equally accurate and efficient. For general 3D problems, the Lagrangian approach is costlier than the Eulerian approach owing to the interpolation on curvilinear geometries. Moreover, the Eulerian approach is much easier to implement in a CFD code. Hence, we use this approach for all the problems discussed in section 2.6.

2.5.3 Numerical issues

Numerical issues occur primarily due to the presence of second gradients of velocity in the model. To obtain numerically convergent results, we use a small under-relaxation on η_2 as follows:

$$\eta_2^{new} = (1 - \alpha_u)\eta_2^{old} + \alpha_u\Omega_{ij}^{mod}\Omega_{ij}^{mod}T^2 \quad (2.29)$$

The under-relaxation factor, $\alpha_u = 0.1$ was used for all the test cases. Another approach is to under-relax the eddy viscosity itself.

The usual definition of timescale in equation 2.26 is

$$T = \max\left(\frac{1}{\beta^*\omega}, 6\sqrt{\frac{\nu}{\beta^*k\omega}}\right) \quad (2.30)$$

This is singular at the wall. The TKE in the $k - \omega$ model behaves as $y^{3.23}$ near a solid wall and ω behaves as $1/y^2$. Hence the second term in (2.26) goes as $1/y^{0.625}$. For a better near-wall behavior, we use $T = \max(T_1, T_3)$ where

$$T_1 = \frac{1}{\beta^* \omega}; \quad T_2 = 6 \sqrt{\frac{\nu}{\beta^* k \omega}}; \quad T_3 = (T_1^n T_2)^{1/n+1} \quad (2.31)$$

with $n = 1.625$ to get $T \propto y$ near the wall.

2.6 Results and discussion

Test cases are chosen in which the effect of rotation and curvature enter the mean flow predominantly through the changes in turbulent stresses. Detailed comparison of both the mean velocity and the skin friction is made with the data from experiments or DNS. Unless otherwise mentioned explicitly, we have used OpenFOAM for all the computations discussed in this section.

2.6.1 Rotating Plane Channel

The flow physics in spanwise rotating channel flow have been studied in a number of experiments and numerical simulations (Johnston et al., 1972; Kristoffersen and Andersson, 1993; Grundestam et al., 2008). For fully developed flow, invoking the parallel flow assumption that U is a function only of y and with an angular velocity, Ω^F , about the spanwise z -axis, the mean U -momentum equation simplifies to

$$0 = -\frac{\partial P^*}{\partial x} + \frac{\partial}{\partial y} \left((\nu + \nu_t) \frac{\partial U}{\partial y} \right) \quad (2.32)$$

where P^* is the effective pressure with the centrifugal force absorbed. The effect of rotation enters the mean flow field only indirectly through the changes in the turbulent stresses modeled in ν_t . The imposed rotation breaks the symmetry of the flow field causing stabilization of the turbulence on one side and destabilization on the other side.

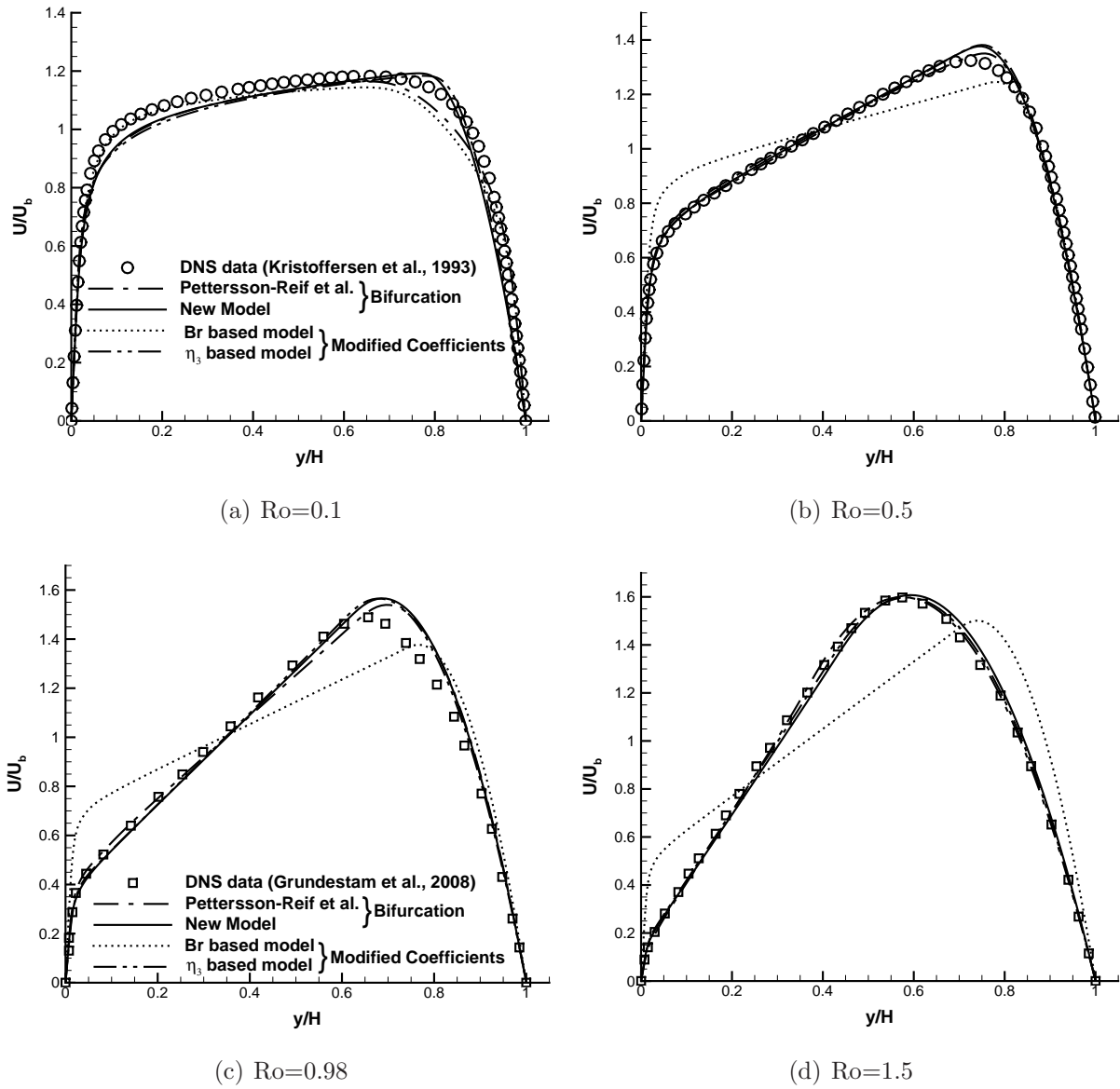


Figure 2.5 Comparison of mean velocity profiles at different rotation numbers

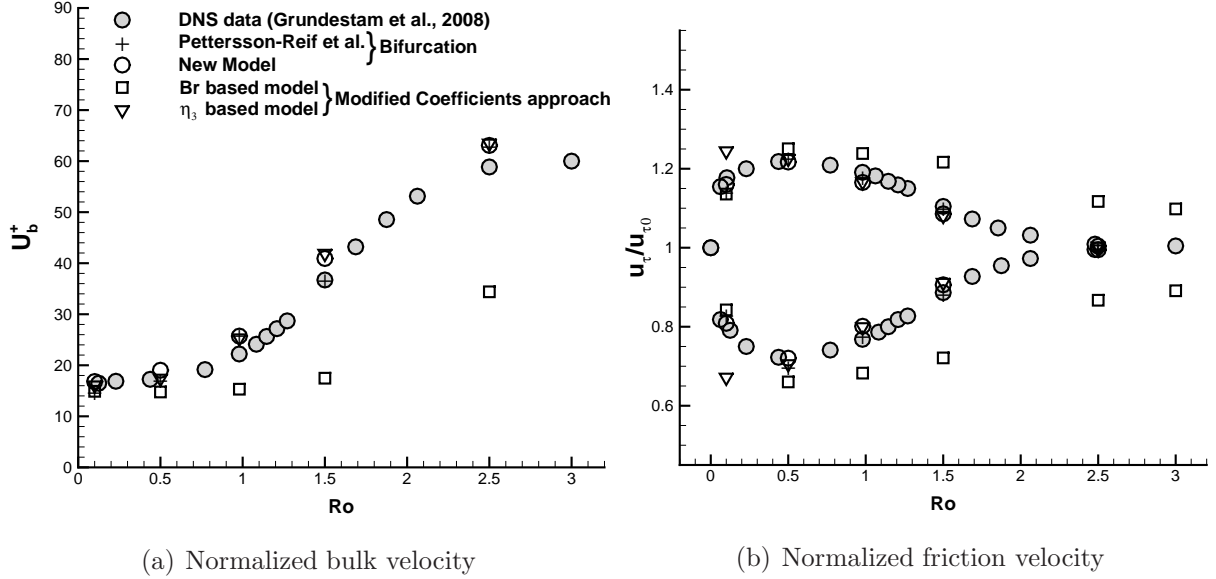


Figure 2.6 Rotating channel flow: Effect of rotation on bulk velocity and friction velocity

The flow conditions for this test case are consistent with the DNS of Kristoffersen and Andersson (1993): $Re_\tau \equiv u_\tau h/\nu = 194$ where h is the channel half-width. The $k-\omega$ model, by design, predicts the near-wall turbulent kinetic energy peak incorrectly. And hence, we limit our comparisons to the mean velocity and skin friction.

Fig. 2.5 compares the mean velocity profiles predicted by curvature models with the DNS data of Kristoffersen and Andersson (1993) and Grundestam et al. (2008). The results show excellent agreement with the DNS data. On the “stable” side of the channel, the frame rotation is in the direction opposite to the background shear; hence, the eddy viscosity is reduced due to the suppression of turbulence. This reduces the resistance to the flow thereby increasing the velocity. On the “unstable” side, the eddy viscosity is increased due to enhancement of turbulence, resulting in lower velocity. This explains the asymmetry of the velocity profiles in Fig. 2.5. An irrotational core region is observed at the center of the channel where $dU/dy = 2\Omega^F$. It is in agreement with the linear stability theory – the irrotational core region corresponds to neutral stability.

At $Ro=0.1$, all the rotation correction models agree well with the DNS data. At

high rotation numbers, the Br based model fails to respond adequately. Pettersson-Reif et al. (1999) and both the proposed models show good agreement. As the rotation rate increases, the flow tends to relaminarize. The velocity profiles tend towards parabolic, as shown in Fig. 2.5. The skin friction decreases allowing higher bulk velocities. This trend is captured very well by the proposed models as shown in Fig. 2.6. The normalized friction velocity trend with increasing Rotation numbers is also in good agreement with the DNS data. We predict complete relaminarization at $Ro=2.5$ — a bit earlier than that observed by Grundestam *et al.*. The skin friction loop is unclosed for the Br based model even at $Ro = 3.0$, which means that relaminarization occurs at much higher rotation numbers with this model. With reference to Figs.1&2 of Smirnov and Menter (2009), the proposed models in this paper are as accurate as the Spalart-Shur correction to the SST $k - \omega$ model.

To understand where the rotation effects appear inside the boundary layer, the rotation correction factor is plotted as a function of wall distance normalized with friction velocity, $y^+ = yu_\tau/\nu$ for $Ro = 0.1$ in Fig. 2.8. A bifurcation based model is used and hence, $C_\mu^* > 1.0$ signifies the unstable side and $C_\mu^* < 1.0$ signifies the stable side. We find that the model is active immediately outside the viscous sub-layer. The dominant effect occurs around $y^+ \approx 30$. At a higher rotation number of $Ro = 0.5$, however, the rotation effect appears immediately close to the wall on the stable side and the recovery is much slower into the center of the channel compared to that at a low Rotation number. At $Ro = 0.1$, the recovery of the destabilizing effect is slower than of the stabilizing effect.

2.6.2 Curved wall boundary layer

In analogy with rotation, streamline curvature can have profound influence on the flow field. Convex curvature suppresses the turbulence whereas concave curvature enhances it. In the case of convex curvature, the flow rotation is in the same direction as the rotation of the velocity vectors. For concave curvature, the two directions are opposite. Co-

rotation stabilizes the turbulence, counter-rotation enhances it (Durbin, 2011). When the turbulence is suppressed, there will be less mean momentum transport from the freestream to the surface of the wall. Hence, wall shear decreases significantly and the tendency for the flow to separate increases. When the turbulence is enhanced, wall shear increases because of the increased turbulent mixing.

The governing equations for the mean flow in local plane polar coordinates, invoking the boundary-layer approximation are (Durbin, 1993)

$$\begin{aligned} \frac{U}{\alpha} \frac{\partial U}{\partial x} + V \frac{\partial U}{\partial y} &= -\frac{1}{\alpha} \frac{\partial P}{\partial x} + \nu \frac{\partial^2 U}{\partial y^2} - \frac{\partial \overline{uv}}{\partial y} - \frac{2\overline{uv}}{\alpha R_c} \\ \frac{U^2}{\alpha R_c} &= \frac{\partial(P + 2k/3)}{\partial y}; \quad \frac{\partial U}{\partial x} + \frac{\partial \alpha V}{\partial y} = 0 \end{aligned} \quad (2.33)$$

where $\alpha = 1 + y/R_c$ and $\overline{uv} = -\nu_t[\partial_y U - U/(\alpha R_c)]$. Here x denotes a direction parallel to the surface and U is the mean velocity in the x -direction; y denotes a direction normal to the boundary surface and V is the mean velocity in the y -direction. R_c is the radius of curvature of the surface and δ is the 99% boundary layer thickness. The above equations are solved by a spatial marching technique. $R_c/\delta = \infty$ for a flat plate boundary layer, $R_c/\delta > 0$ for convex wall and $R_c/\delta < 0$ for concave wall. Abrupt changes of surface curvature cause discontinuities, but the effect dies away quickly (Durbin, 1993). At the wall, a no-slip boundary condition is imposed with specific dissipation rate $\omega = 60\nu/[\beta(\Delta y)^2]$. At the freestream, $\partial_y U = -1/(\alpha R_c)$, $k = 10^{-5}U_\infty^2$ are imposed. For specific dissipation rate at the freestream (Menter, 1992)

$$\omega = \frac{4}{\beta^*} \frac{u_\tau^2}{U_{freestream} \delta^*} \quad (2.34)$$

2.6.2.1 Convex

Curvature is always associated with pressure gradients. To assess the curvature corrections, we use experiments of Gillis et al. (1980) and Simon et al. (1982) in which curvature effects are isolated by maintaining zero surface pressure gradient on the test

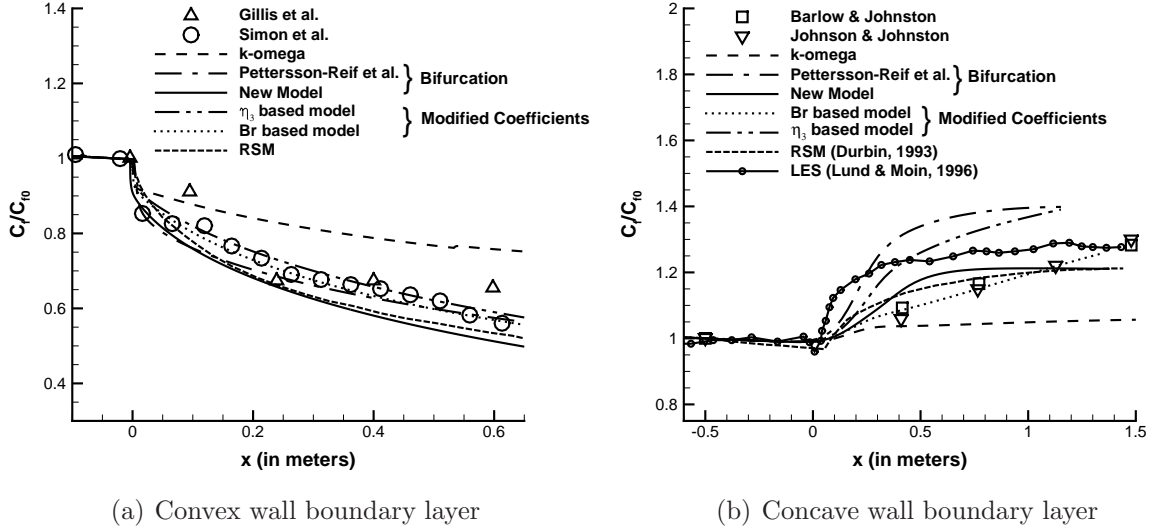


Figure 2.7 Skin friction plotted along the curved walls

wall. This was achieved by contouring the outer wall appropriately. The experimental set-up consists of a developing flat plate boundary layer which enters, at $Re_\theta = 4200$, a 90° constant-curvature bend with $\delta_{99}/R_c = 0.1$. Gillis et al. inferred the skin friction from the velocity measurements. But, we also compare with Simon et al. who measured the heat transfer coefficient, invoking Reynold's analogy.

Fig. 2.7 compares the different curvature models with the experimental data and with an SMC model (Durbin, 1993). The $k - \omega$ model without curvature corrections underpredicts the effects of curvature. When a curvature correction is added, agreement with the data is improved.

2.6.2.2 Concave

Johnson and Johnston (1989) and Barlow and Johnston (1988) studied the effect of concave curvature on turbulence using a free-surface water channel. Similar to the Gillis et al., the pressure over the concave surface is maintained constant. The flow enters the curved section at $Re_\theta = 1140$ and the bend has a curvature of $\delta_{99}/R_c = 0.05$. Fig. 2.7 shows the comparison of the model predictions with the experimental data. The influence

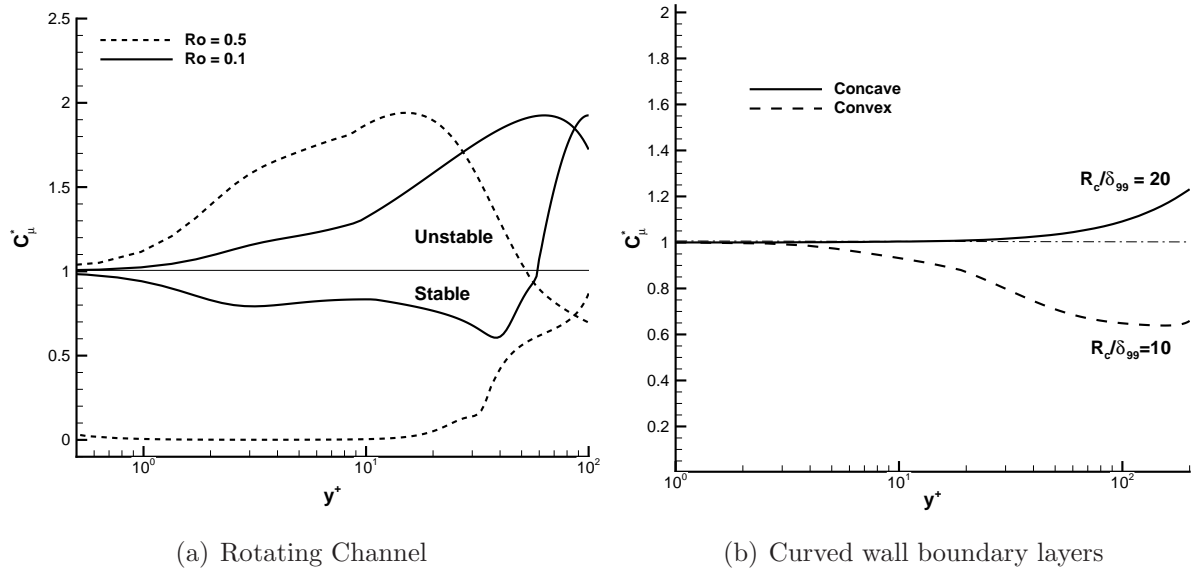
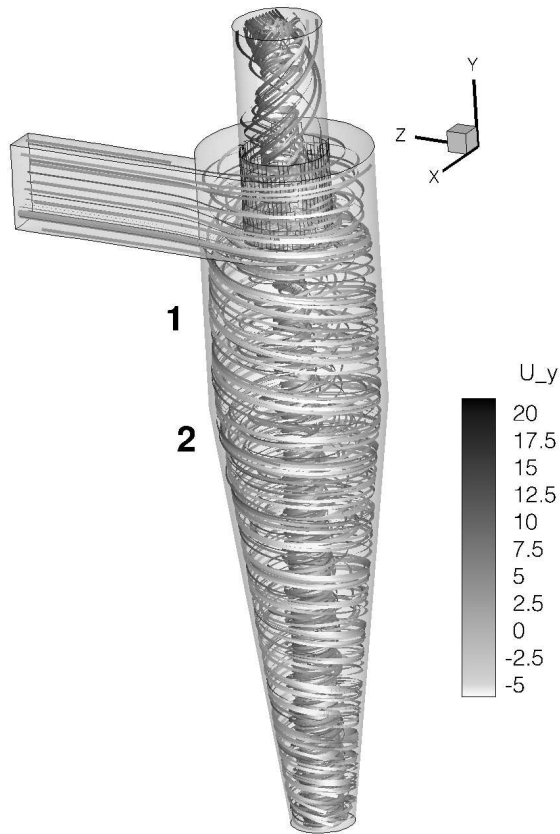


Figure 2.8 Variation of rotation/curvature correction factors inside the boundary layer on the velocity profile is small. But, the skin friction increases significantly from the flat plate value. The skin friction data are inferred from the velocity profiles using a Clauser chart; but, LES of Lund and Moin (1996) suggest that the Clauser method could be in error. We also plotted their LES data. Qualitatively, the curvature models showed correct behavior for concave curvature.

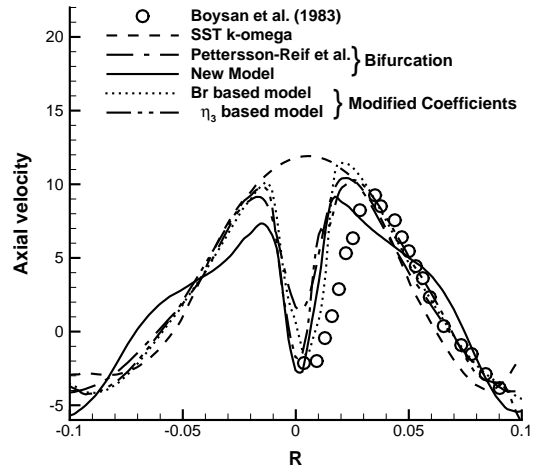
To understand where the curvature effects are predominant inside the boundary layer, we plotted the curvature correction factor in Fig. 2.8 for the bifurcation based model. The models are active for $y^+ > 10$. The dominant effect occurs for $y^+ > 30$ for both concave and convex curvatures. This is consistent with observations in the rotating channel flow.

2.6.3 Hydrocyclone

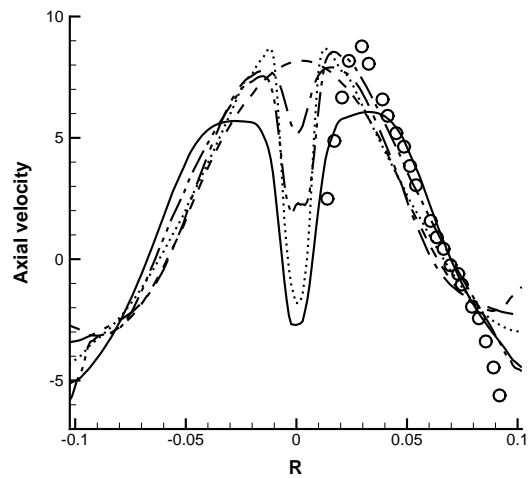
Flow through a hydrocyclone is characterized by strongly swirling motion as shown in Fig. 2.9. Swirl induced suppression of turbulence results in a downward flow near the axis of the hydrocyclone. This cannot be predicted by the scalar eddy viscosity closures. Predicting downward flow is critical in the design of Hydrocyclones as it determines the



(a) Volume ribbons showing strongly swirling flow in Hydrocyclone. Ribbons are colored by axial velocity.



(b) Station1



(c) Station2

Figure 2.9 Hydrocyclone: Axial velocity profiles at two different stations indicated on the left

separation efficiency of these devices.

We use a typical high-efficiency cyclone design of Stairmand, with a diameter of 0.205 *m*. Experimental data are from Boysan et al. (1983). The steady Navier-Stokes equations are solved using an incompressible solver in OpenFOAM. The cyclone inlet velocity corresponds to the volumetric flow rate of 0.08 m^3s^{-1} (Slack et al., 2000). At the outflow, atmospheric pressure is specified. The bottom is closed.

The flow enters the hydrocyclone tangentially at the inlet. The vortex that is created undergoes stretching due to the contraction and hits the closed bottom, then reverses it's direction towards the vortex finder at the top. Due to the swirl, a low-pressure core forms at the center of the hydrocyclone allowing a downward flowing stream near the axis. Hence, the axial velocity contains zones of upward and downward flow. Rayleigh's centrifugal stability criterion explains the physics behind the effect of swirl in the vortex core (Durbin and Medic, 2007). From radial equilibrium,

$$\frac{\partial p}{\partial r} = \frac{u_\theta^2}{r} = \frac{L^2}{r^3} \quad (2.35)$$

where v_θ is the tangential velocity and $L = rv_\theta$ is the angular momentum. The stability criterion is that if $\partial L^2/\partial r > 0$, the flow is stable. The tangential injection of the flow ensures that this criterion is satisfied. And hence, turbulence is suppressed providing a path of low resistance for the downward stream.

The RANS simulations are carried out with different curvature models and the axial velocity at two different stations along the axis of hydrocyclone are compared with the experimental data in Fig. 2.9. The original SST $k - \omega$ model could not predict the downward flow at the core. All the curvature corrections show significant improvement over the original model.

2.6.4 Serpentine Channel

The serpentine channel has both convex and concave curvatures (see Fig. 2.10) and when subjected to spanwise rotation, the separation bubble in the bends 1 and 2 dif-

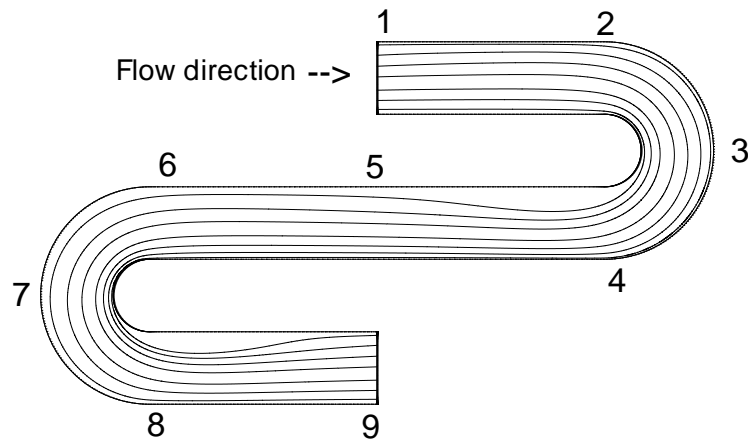


Figure 2.10 Flow configuration of serpentine channel

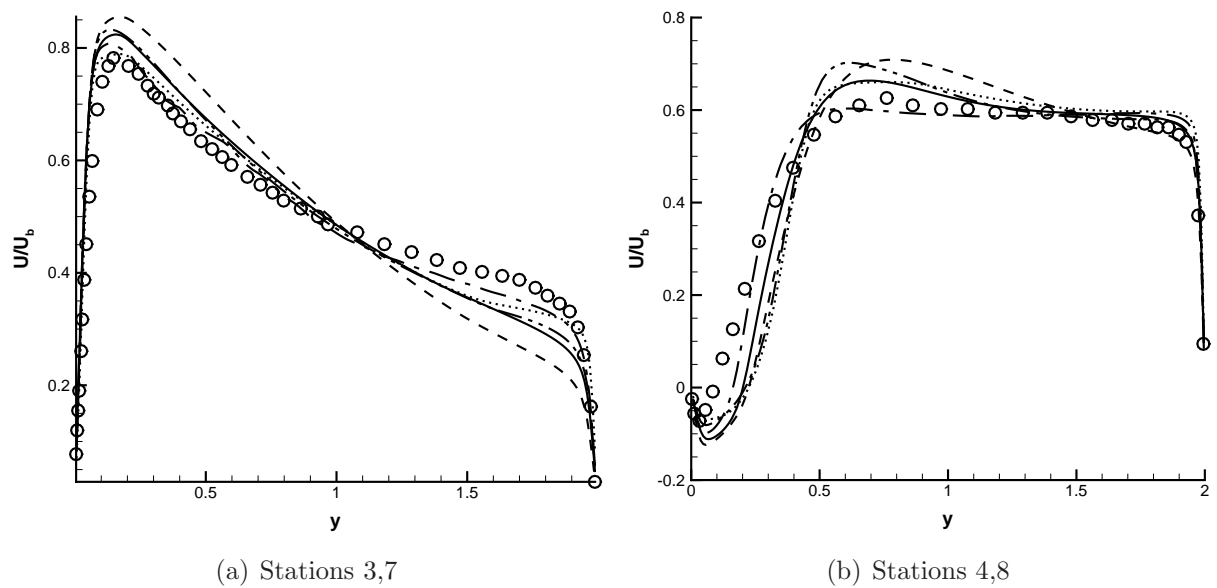


Figure 2.11 Serpentine Channel, stationary: Comparison of mean velocity profiles with Laskowski and Durbin (2007) data. For the legend, see Fig. 2.13

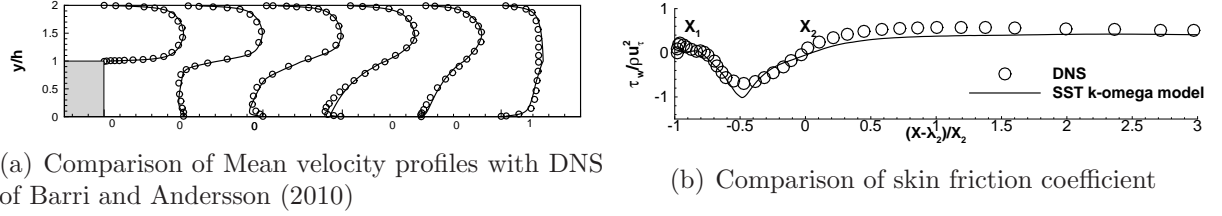


Figure 2.12 Backward-facing step, non-rotating case

fer. Recent DNS data from Laskowski and Durbin (2007) is used for comparison. The Reynolds number is $Re = 2\delta U_b/\nu = 5600$ where δ is the channel half-width. The curvature of the bend is $R_c/\delta = 2.0$. These simulations are attractive for their streamwise periodic inflow boundary conditions. Experimental data available for similar test cases require specification of accurate inflow boundary conditions consistent with the experimental set-up which is challenging. Periodicity between exit and inflow is invoked for the velocity, as in the DNS. In this work, we present the stationary case in this subsection.

The key difference between the Serpentine channel and the curved wall boundary layers is that the effect of pressure gradient is present in the former, in addition to the effect of curvature. In analogy with flow over a cylinder, the flow accelerates over the first half of the inner curved wall (convex) and decelerates over the second half. On the outer curved wall (concave), the flow decelerates over the first half and accelerates in the second half. The deceleration results in adverse pressure gradients and the flow is susceptible for separation. On the convex wall, the turbulence levels are suppressed and hence the flow cannot sustain the adverse pressure gradients and separates in the later half of the bend.

The mean velocity profiles at two different stations for the stationary case are plotted in Fig. 2.11 show that all the curvature corrections predict similar flow features. Petterson-Reif et al. (1999) gives slightly better agreement compared to other models.

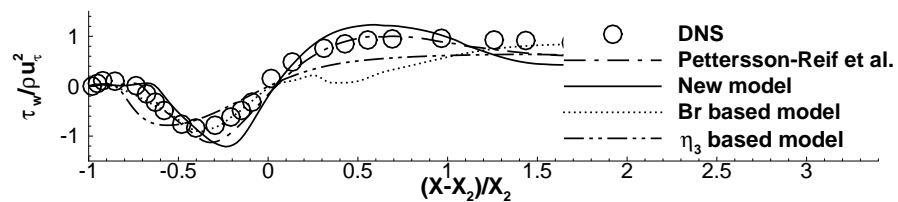


Figure 2.13 Backward-facing step, $Ro=0.05$: Comparison of skin friction coefficient

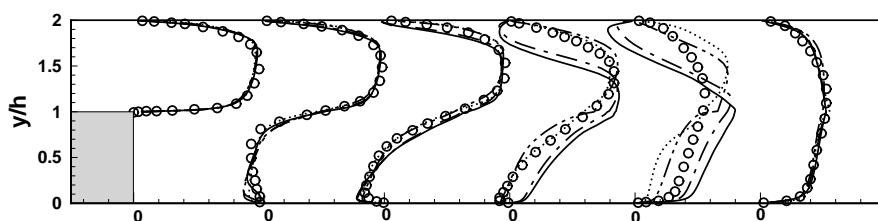


Figure 2.14 Comparison of Mean velocity profiles at $Ro=0.05$

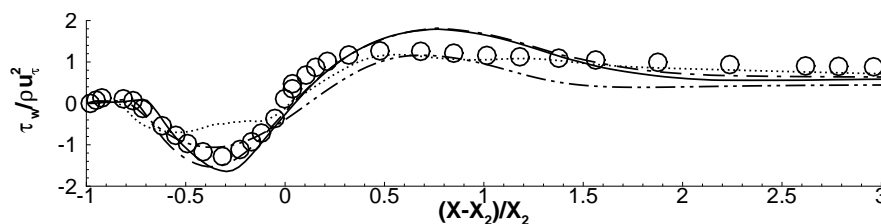


Figure 2.15 Backward-facing step, $Ro=0.2$: Comparison of skin friction coefficient at $Ro=0.2$. For the legend, see Fig. 2.13

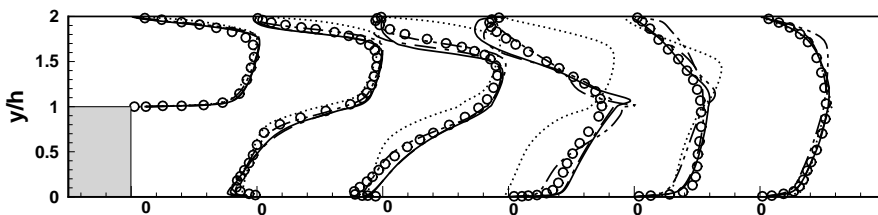


Figure 2.16 Comparison of Mean velocity profiles at $Ro = 0.2$

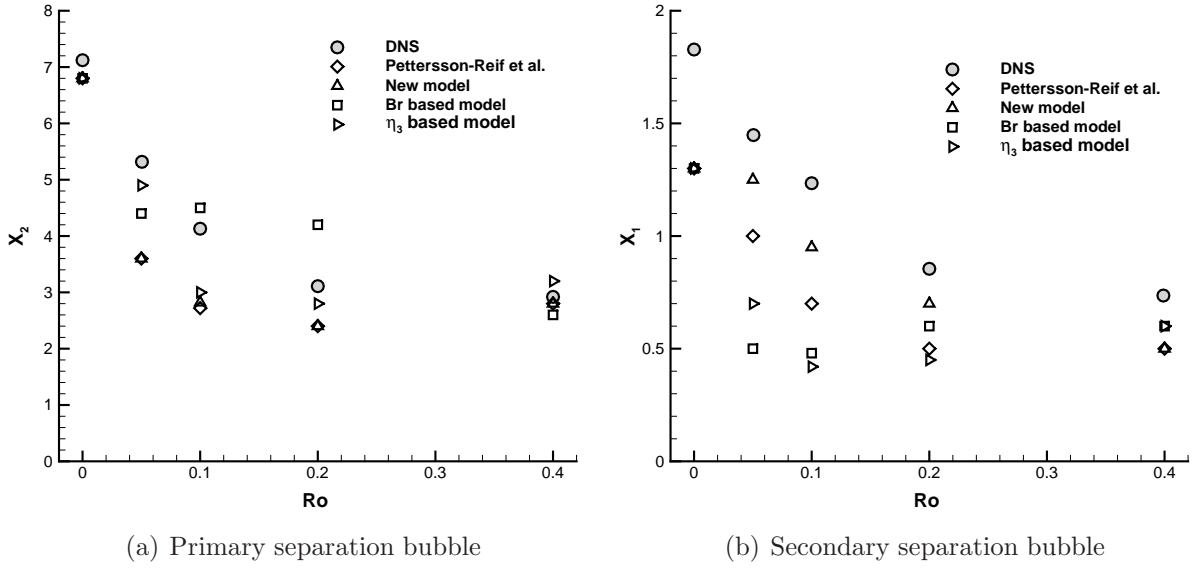


Figure 2.17 Reattachment length plotted as a function of rotation number. For X_1 and X_2 , see Fig. 2.12

2.6.5 Rotating Backward-facing step

The rotating backstep is a configuration which brings out the effect of spanwise rotation on the separation and reattachment of the free-shear layer downstream of the step. If the rotation is in the direction of mean shear, the turbulent mixing is enhanced and the size of the recirculation bubble is decreased. If the rotation is anti-parallel to the direction of mean shear, the turbulent mixing is suppressed and the size of the recirculation bubble increases. We use recent DNS data of Barri and Andersson (2010) at $Re = U_b(H - h)/\nu = 5600$ to assess the rotation corrections on this complex flow configuration. The expansion ratio is $ER = H/(H - h) = 2$ with h being the step height and H being the downstream height of the channel. Following the DNS set-up, the spanwise rotation is imposed such that the turbulence over the stepped wall is enhanced and that over the opposite wall is suppressed.

A recycling inflow boundary condition is used so that fully developed turbulent conditions can be achieved upstream of the step. At the outflow, a pressure gradient in the

wall-normal direction is imposed to balance the Coriolis force:

$$\frac{\partial P}{\partial y} \approx -2\Omega^F U \quad (2.36)$$

The definition of rotation number is, $Ro = \Omega^F(H - h)/U_{b0}$. U_{b0} is the bulk velocity upstream of the step in the non-rotating case. However, note that the local rotation number in the downstream part of the channel is 4 times greater than upstream because the bulk velocity, U_b , downstream of the step is related to that upstream by $U_{b0}(H-h)/H$. Hence, the effect of rotation is much stronger downstream of the step.

In a backstep, the free-shear layer emanating from the step undergoes geometry-induced separation. When subjected to rotation, the turbulence on this wall is amplified. Due to enhanced turbulence levels, higher momentum fluid away from the wall is transported towards the wall. This shortens the reattachment length.

Fig. 2.12 presents mean flow results for the non-rotating case using the SST $k - \omega$ turbulence model. From the mean velocity profiles, it can be observed that the flow reattaches earlier than that predicted by DNS. This is consistent with the skin friction prediction as well. Moreover, post-reattachment the skin friction is not in good agreement with the data. Hence, when evaluating the effectiveness of the proposed rotation corrections, it is important to understand that some discrepancies come from the base turbulence model itself and not the rotation correction per se.

Figs. 2.13-2.16 show the mean velocity profiles and the skin friction variation along the stepped wall at two rotation numbers. The proposed models show good agreement with the data up to the reattachment location. Post reattachment, the agreement is poor. This could be attributed to the base turbulence model itself. At moderately high rotation numbers, DNS data show a separation bubble on the upper wall, opposite to the step. This is due to the stabilizing effect of rotation on that wall. The turbulence is suppressed on this surface and hence the flow is susceptible to separation. Both of the bifurcation models show separation even at low rotation numbers which is not seen in the DNS data. This was not the case when these corrections were used in conjunction

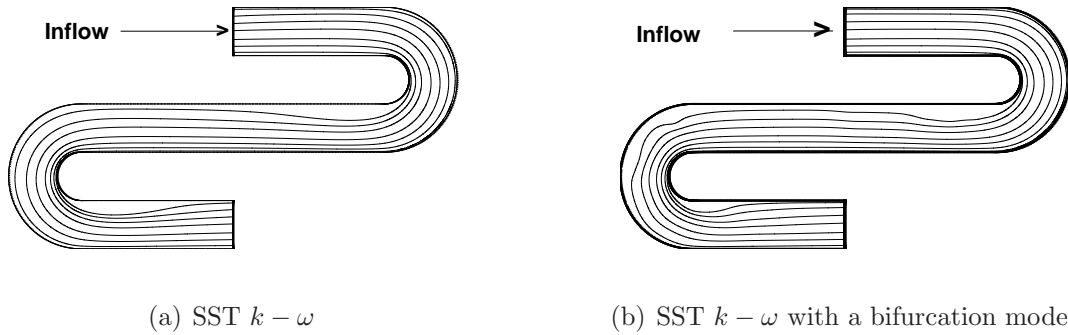


Figure 2.18 Stream traces showing the combined effect of rotation and curvature. The waviness in the streamtraces is because the flow is laminar in that region and the use of turbulence model may not be appropriate.

with $v^2 - f$ model which predicts the correct level of turbulent kinetic energy near the walls (Pettersson-Reif et al., 1999). This could be due to low Reynolds numbers used for the simulation and since using a turbulence model is not appropriate where the flow is laminar. Hence, we focus on the effect of rotation on the free shear layer emanating from the step.

The variation of the reattachment length of both the primary (X_2) and the secondary (X_1) separation bubbles with rotation number is plotted in Fig. 2.17. Both of the models from the bifurcation approach and η_3 based model predict the reattachment length more accurately than the Br based model. A trend of approximately constant reattachment length after $Ro = 0.2$ is captured very well by the models.

2.6.6 Rotating serpentine channel

The serpentine channel has both convex and concave curvatures and when subjected to spanwise rotation, the size of the separation bubble in the two bends differ. Laskowski and Durbin (2007) performed Direct Numerical Simulations on this flow configuration at a Reynolds number, $Re = 2\delta U_b/\nu = 5600$ where δ is the channel half-width. The curvature of the bend is $R_c/\delta = 2.0$. The streamwise periodic inflow boundary condition used in these simulations is particularly attractive for turbulence model validation. The

validation of the models for the stationary case showed consistent improvement (Arolla and Durbin, 2013a). When the spanwise rotation is imposed, the outflow pressure has to be specified such that the wall-normal pressure gradient balances the Coriolis force. The direction of rotation is consistent with the DNS set-up. In the first bend, the rotation aides the curvature and in the second bend the rotation opposes the curvature. When the rotation aides curvature, the turbulence levels on the convex wall (bend 1) are suppressed leading to earlier separation and larger separation bubble. When rotation opposes curvature, the turbulence levels are increased leading to a shortened separation bubble in bend 2. This qualitative behavior is predicted well by the bifurcation model where as the original SST $k - \omega$ is insensitive to the rotation(see Fig.2.18). It can also be observed that the rotation/curvature model predicts separation on the outerwall in bend 2; that is not seen in DNS. Due to this separation, the mean velocity profiles do not agree well with the DNS (not shown). So, this testcase remains a challenge for the rotation/curvature model.

2.6.7 Rotating U-duct

With an objective to test the rotation/curvature correction in a U-duct configuration at high Reynolds numbers, we have chosen the Cheah et al. (1996) set-up. The Reynolds number for this case is, $Re = 2\delta U_b/\nu = 100,000$ where δ is the half-width of the duct and the curvature of the bend is $R_c/\delta = 1.3$. Iacovides et al. (1996) have studied Algebraic Second-Moment Closures (ASM) on this configuration. They concluded that, when the curvature and Coriolis forces reinforce each other, the models predicted satisfactory results of the flow development. But, when the curvature and Coriolis forces oppose each other, the models did not show good agreement with the data. Guleren and Turan (2007) performed Large Eddy Simulation (LES) on this case and showed reasonable agreement for the mean flow characteristics. We use both the LES and experimental data for comparison.

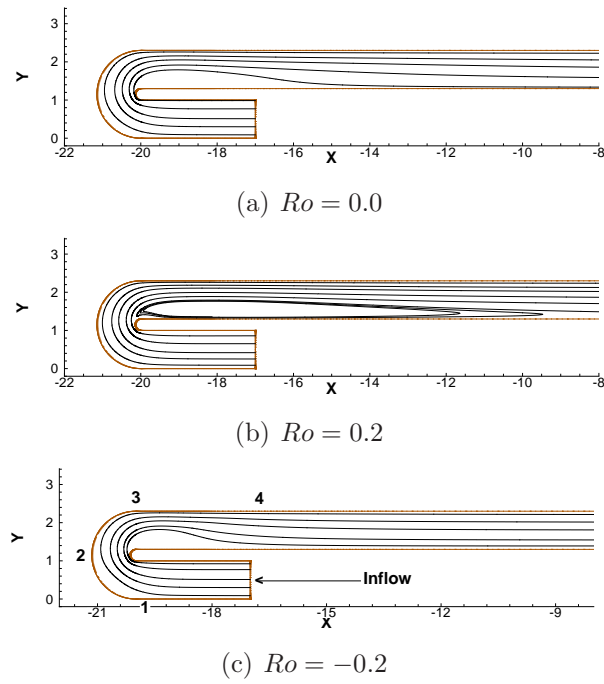


Figure 2.19 Stream traces at different rotation numbers

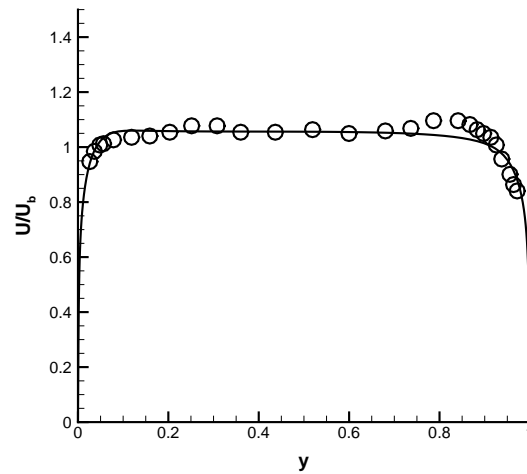


Figure 2.20 Inflow mean velocity profile. Symbols: Experimental data of Cheah et al. (1996); Solid line: Computed

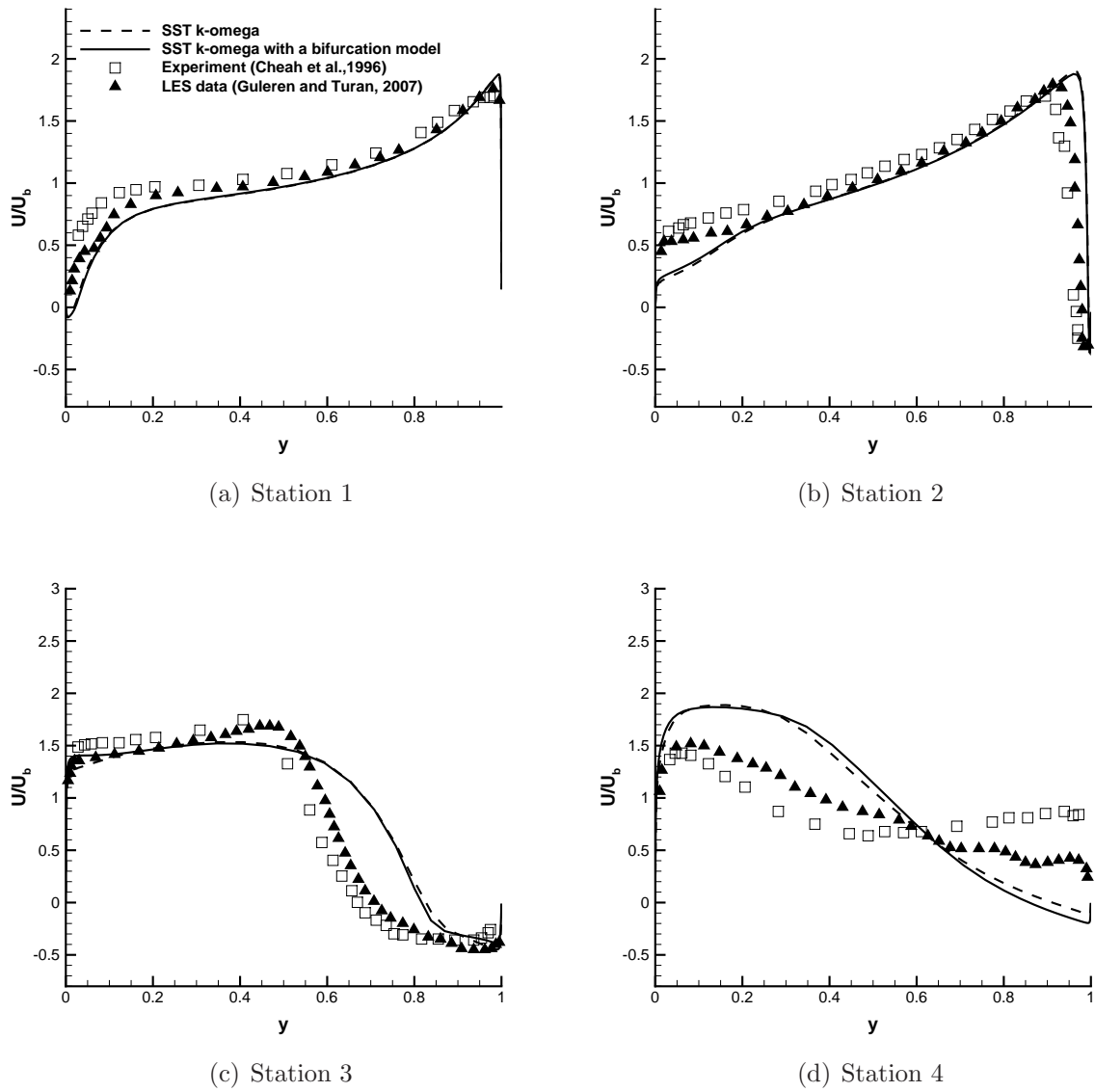


Figure 2.21 Mean velocity profiles at $Ro = 0.0$. For station numbers, see Fig. 2.19

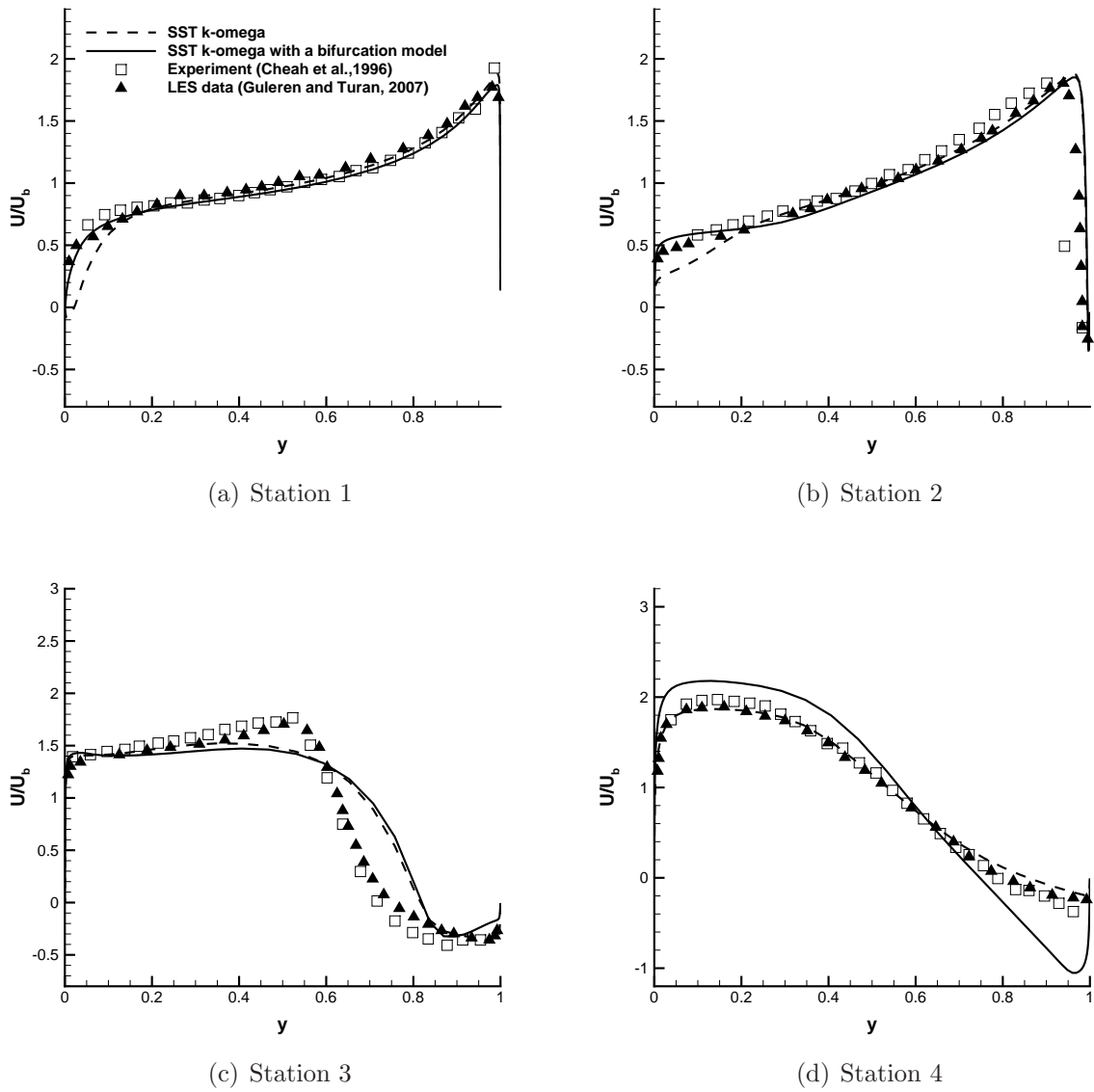


Figure 2.22 Mean velocity profiles at $Ro = 0.2$. For station numbers, see Fig. 2.19

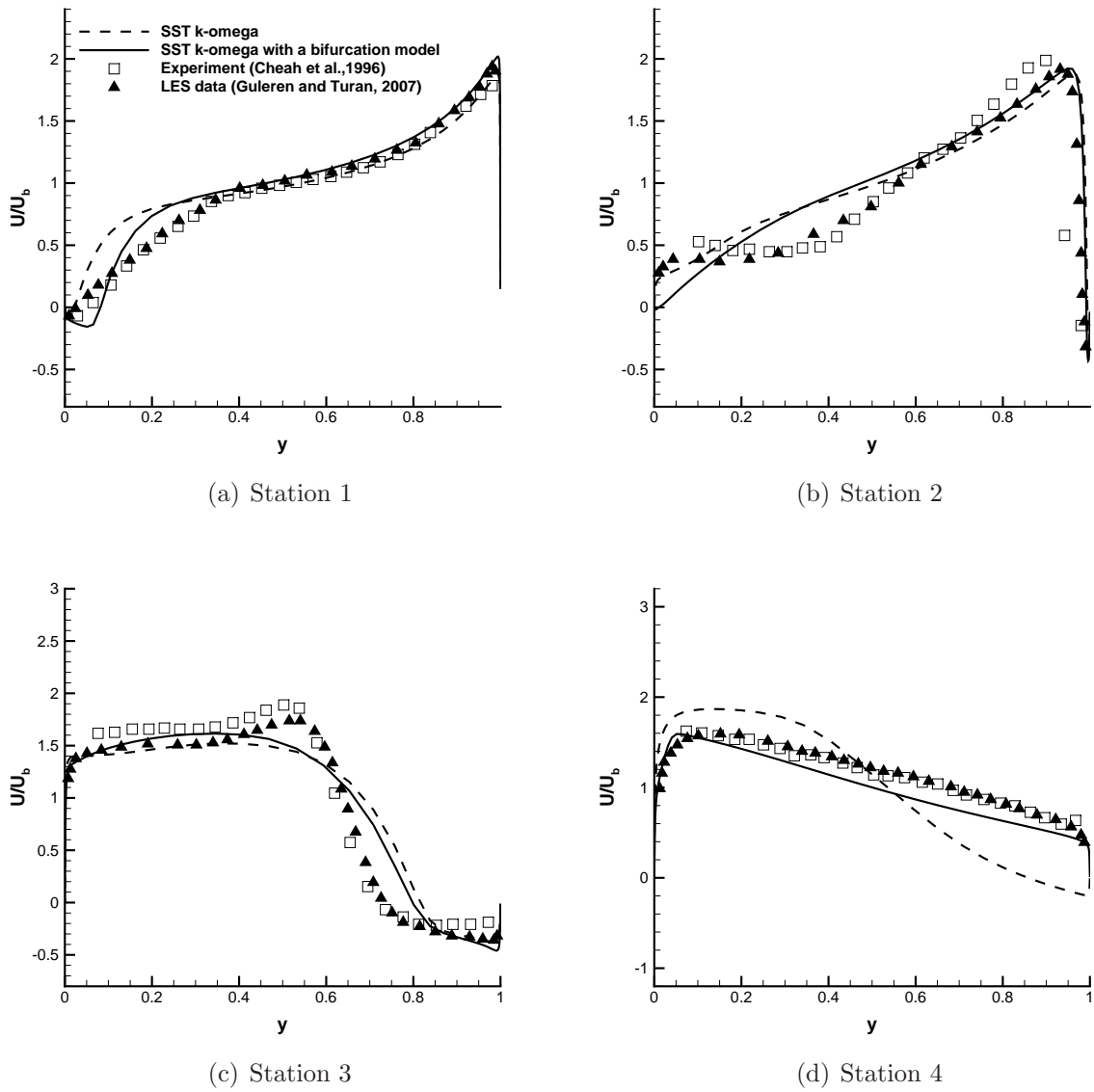


Figure 2.23 Mean velocity profiles at $Ro = -0.2$. For station numbers, see Fig.2.19

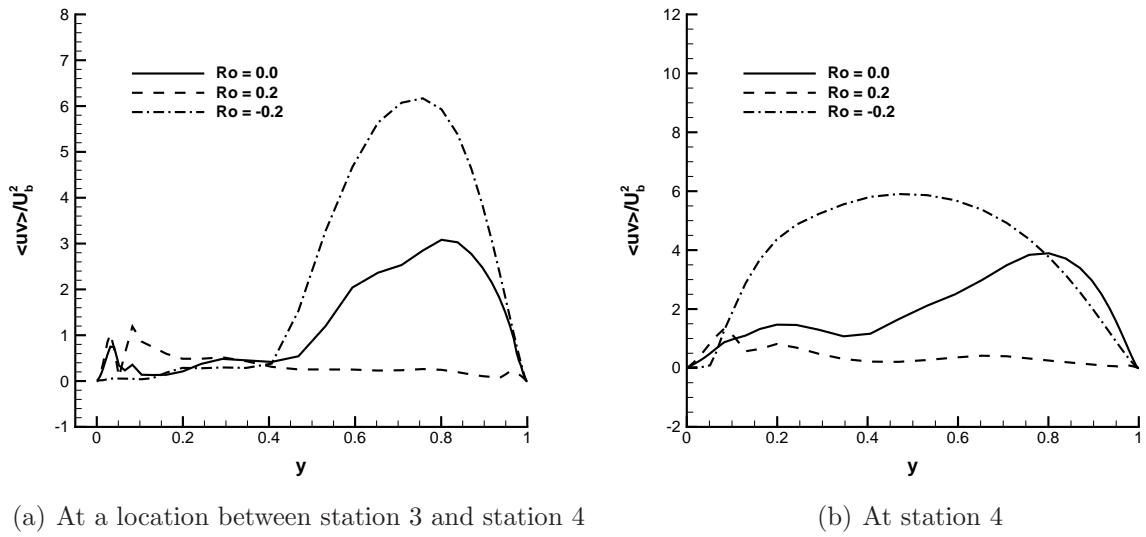


Figure 2.24 Turbulent shear stress profiles downstream of the bend. For station numbers, see Fig.2.19

Fig.2.20 shows the inflow profile generated in a stand-alone channel flow simulation. The boundary layer thickness is different on the two walls which pose challenges in setting up this problem consistent with the experiments. So, it should be noted that some errors in the results can be attributed to the specified inflow profile itself.

In the stationary case, as shown in Fig.2.21, the flow deceleration at the entrance of the bend is overpredicted by the models resulting in small separation. But, note that LES also has difficulty in this region. The flow development in the bend and downstream of the bend does not agree with the bifurcation model. The improvement over the base turbulence model for this case is very small.

However, in the positive rotation case shown in Fig.2.22, the flow development in the bend is accurately captured by the bifurcation model. Downstream of the bend, the model is not accurate. In the negative rotation case, the agreement is poor in the bend, but reasonable downstream of the bend (see Fig.2.23). These results are consistent with the conclusions from Iacovides et al. (1996) with the ASM closures. Overall, it can be concluded that the modeling needs to be refined for the case with combined effects of

rotation and curvature. Fig.2.19 shows the streamtraces in the stationary and the two rotation cases. The qualitative behavior is consistent with the experimental observations. The Reynolds shear stress profiles plotted in Fig.2.24 shows the turbulence enhancement and suppression when the frame rotation is imposed.

2.6.8 Circulation control airfoil

C_j (approx.)	$U_{j,max}$	U_{inlet}
0.12	210	6.924

Table 2.3 Flow conditions

Model	Lift coefficient
LES (Nishino et al., 2010)	3.5
SST k- ω	4.40
Bifurcation model	3.91
Modified coefficients model	4.13

Table 2.4 Lift coefficient predictions at $C_j = 0.12$

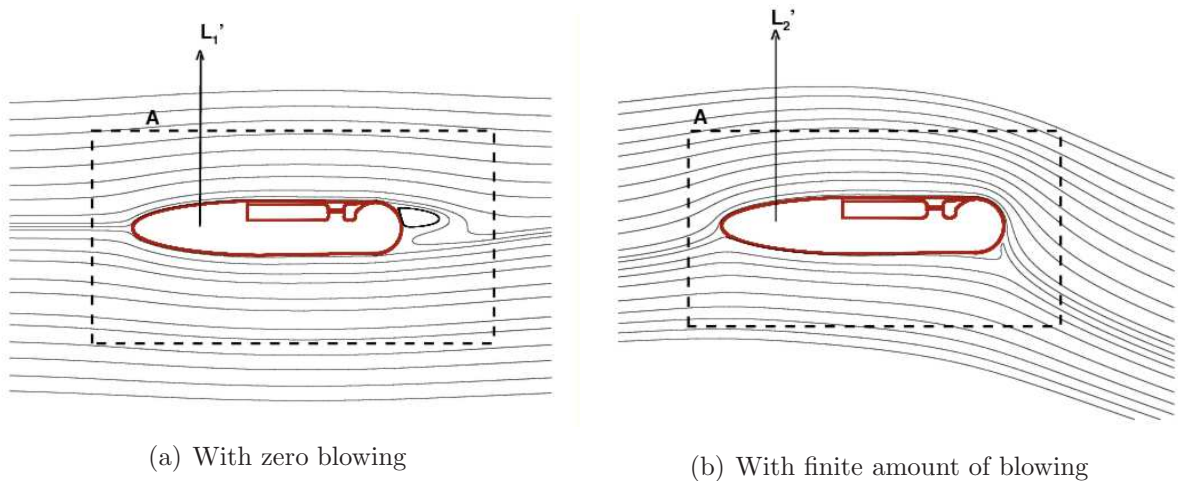


Figure 2.25 Lift enhancement by blowing a jet over the trailing edge: $L'_2 > L'_1$

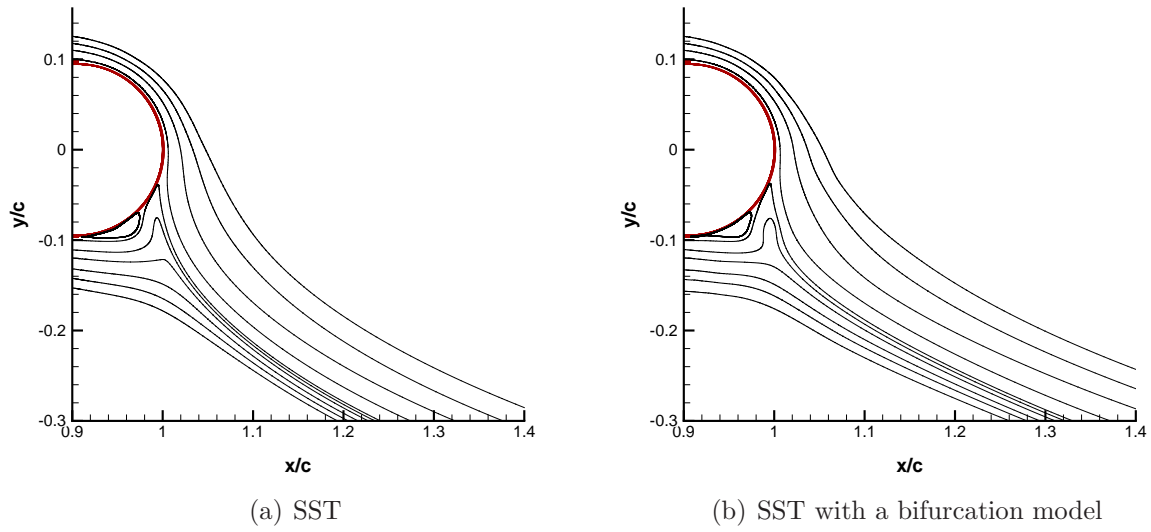


Figure 2.26 Case: $C_j = 0.12$, Stream traces over the Coanda surface

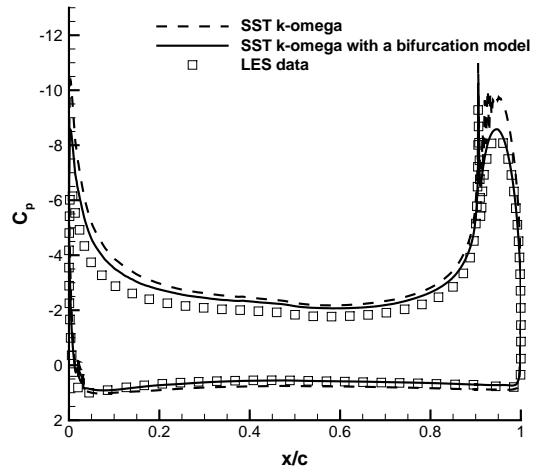


Figure 2.27 Pressure coefficient over the airfoil surface

The geometry is an airfoil configuration in which a tangential jet is blown over a thick, rounded trailing edge to delay separation using the Coanda effect (see Fig.2.25). Highly curved, recirculation regions are seen to form near the trailing edge. We use the LES data from Nishino et al. (2010) for assessing the streamline curvature effects. The simulations were performed at a chord based Reynolds number of 0.49×10^6 and at a jet momentum coefficient of $C_j = \dot{m}_j U_{j,mean} / (q_\infty A) = 0.12$ where $q_\infty = \rho U_\infty^2 / 2$, A is the planform area. The subscript 1 denotes freestream conditions and j denotes jet exit conditions.

Due to sufficiently high Reynolds numbers, the external flow around the airfoil is fully turbulent. When the suction surface turbulent boundary layer interacts with the wall jet from the plenum chamber, the jet transitions to turbulence. Therefore, the transition characteristics of the jet over the Coanda surface are assumed to be unimportant. Several things are important to understand the aerodynamic characteristics of the circulation control airfoil: the interaction of the turbulent wall jet with the suction surface boundary layer, the dynamics of flow separation and reattachment over the curved surface, and the spreading of the jet sheet downstream of the airfoil. A turbulent wall jet can be thought of as a two-layer shear flow: in an inner layer, the flow exhibits similarities in structure with the conventional turbulent boundary layer; and in an outer layer, the shear-layer character is more like free-shear flow. For the turbulent wall jet over a convex surface, the turbulent transport is enhanced in the outer region and diminished in the inner region Launder and Rodi (1983). The Coanda surface is convexly curved and hence predicting both stabilizing and destabilizing effects on turbulence determines the separation location and the jet spreading rate.

The boundary conditions used are: freestream velocity of 34m/s at the inflow and, at the plenum inlet, the velocities given in the table 2.3. The walls of the plenum and the airfoil surface are treated as no-slip boundaries. A slip wall boundary condition is imposed on the tunnel walls. The simulations are run to the atmospheric pressure at the

exit.

At $C_j = 0.12$, the streamtraces plotted in Fig.2.26 clearly show that the curvature correction moves the separation location slightly up over the Coanda surface. The pressure coefficient near the trailing edge is accurate compared to the LES data (see Fig.2.27). The lift coefficient given in table 2.4 shows that there is about 12% improvement when a curvature correction is used. The discrepancies in predicting the suction peak could be the reason for the difference between lift coefficient predicted by RANS model with a curvature correction and LES. This problem is observed even at a lower jet momentum coefficient as well (Arolla and Durbin, 2013b). Further investigation is necessary to address this issue.

2.6.9 Tip leakage vortex

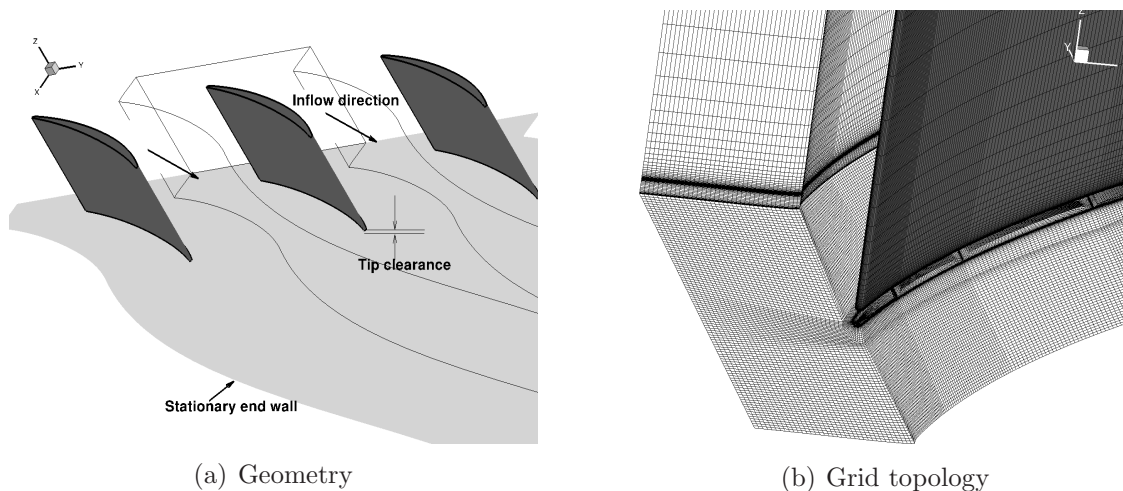


Figure 2.28 Tip leakage vortex: Flow configuration and grid topology

L_x	L_y (=pitch)	L_z (=span)	tip-gap size	stagger angle
$3.30C_a$	$1.70C_a$	$0.92C_a$	$0.03C_a$	56.9°

Table 2.5 Parameters used in the simulation. C_a is the axial chord and C is the chord of the airfoil with $C_a = 0.546C$.

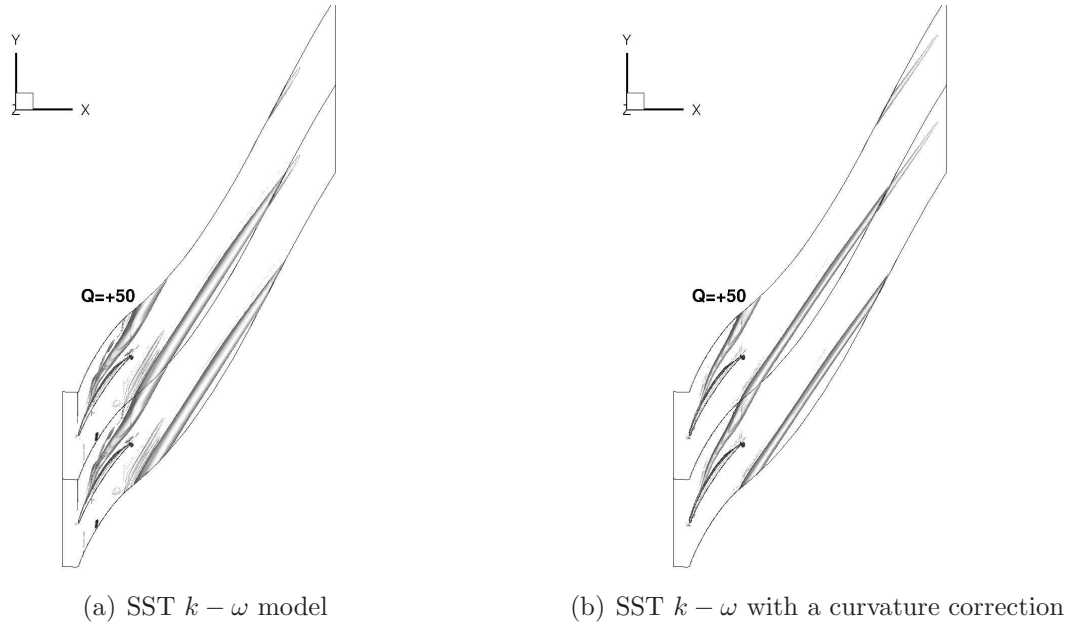


Figure 2.29 Evolution of the tip leakage vortex: Isosurfaces of the vortex core located using Q -criterion ($|\Omega|^2 - |S|^2 = +50$)

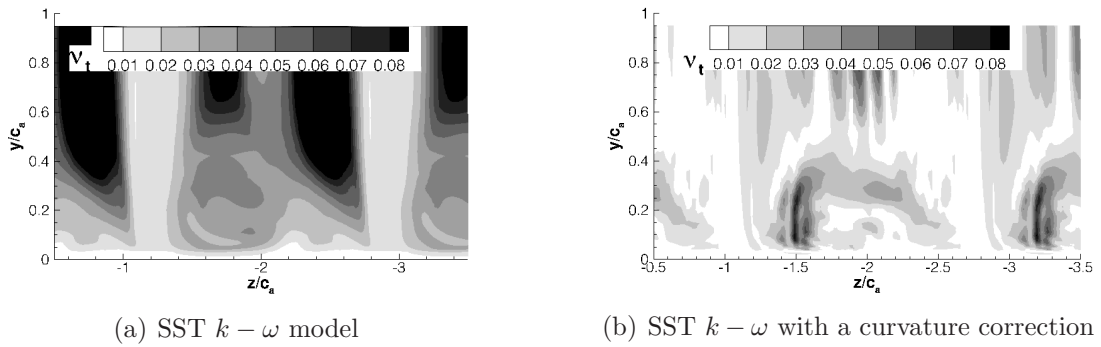
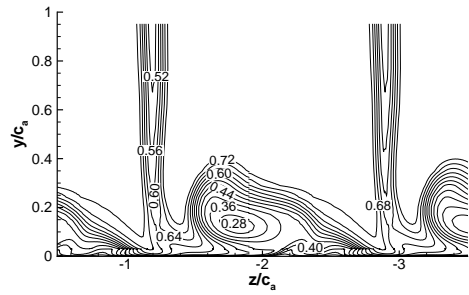
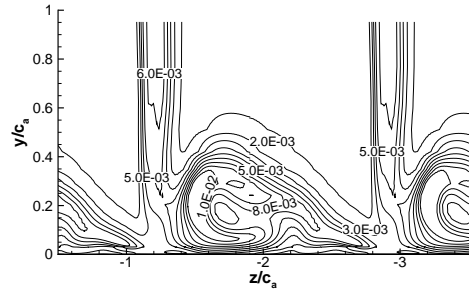


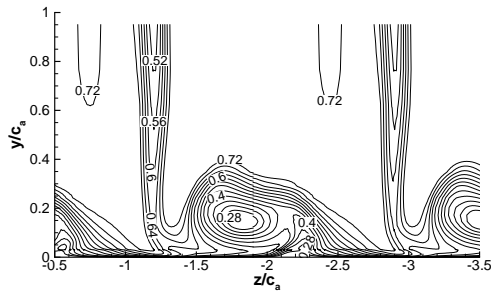
Figure 2.30 Eddy viscosity contours showing the effect of streamline curvature at $X/C_a = 1.366$



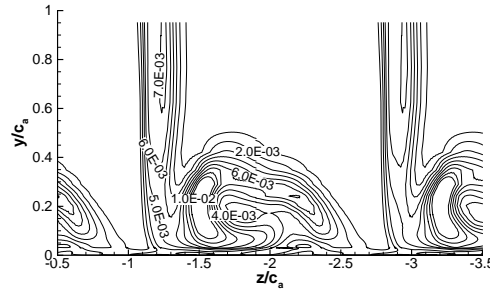
(a) SST $k - \omega$



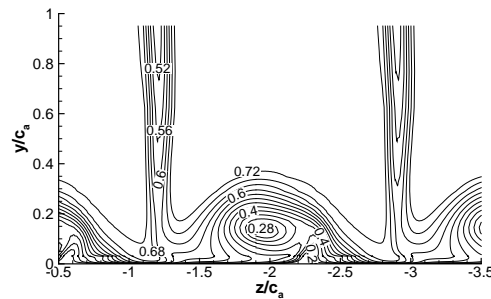
(a) SST $k - \omega$



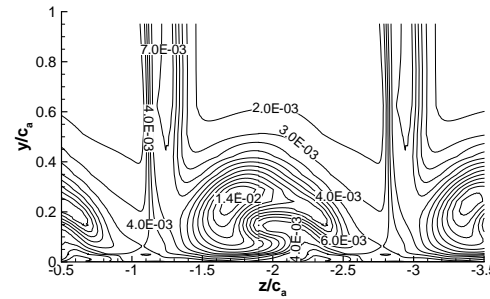
(b) SST $k - \omega$ with a bifurcation model



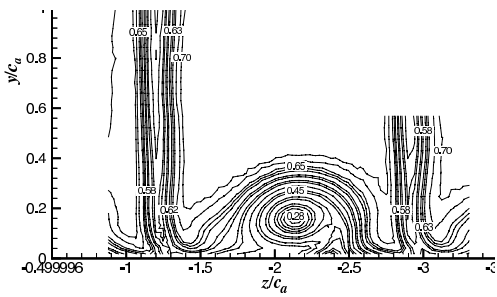
(b) SST $k - \omega$ with a bifurcation model



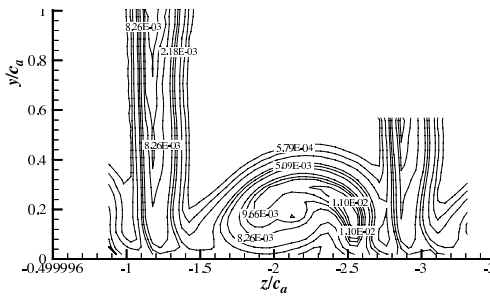
(c) SST $k - \omega$ with a bifurcation model, without DS_{ij}/Dt contribution



(c) SST $k - \omega$ with a bifurcation model, without DS_{ij}/Dt contribution



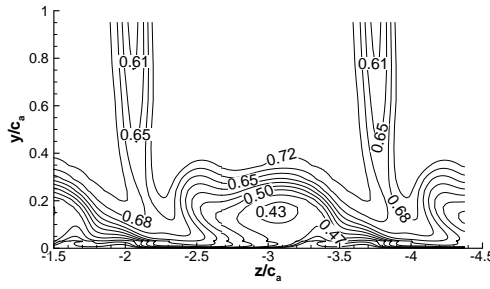
(d) Experimental data



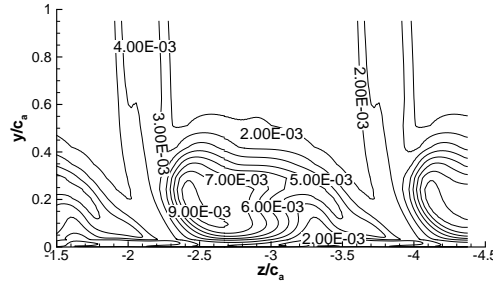
(d) Experimental data

Figure 2.31 Velocity contours

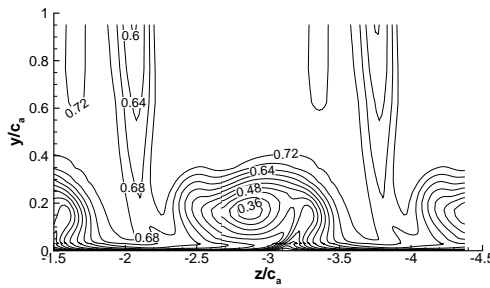
Figure 2.32 TKE contours at $X/C_a = 1.366$



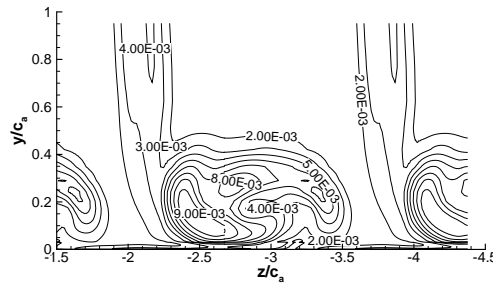
(a) SST $k - \omega$



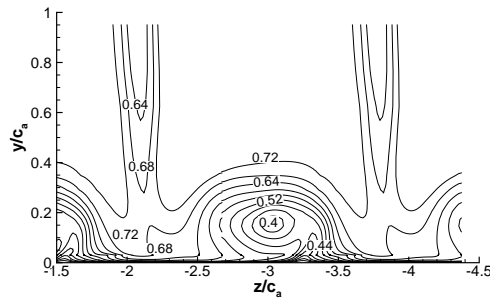
(a) SST $k - \omega$



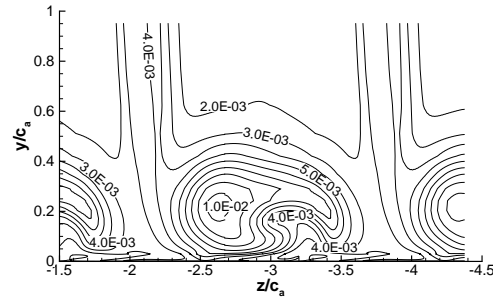
(b) SST $k - \omega$ with a bifurcation model



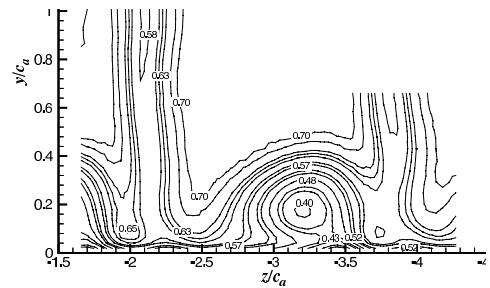
(b) SST $k - \omega$ with a bifurcation model



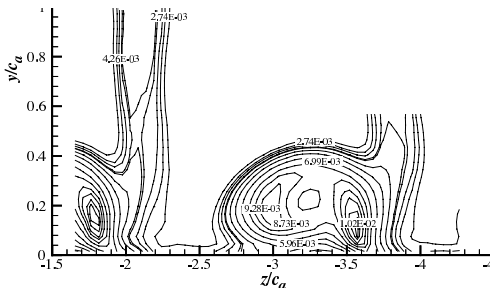
(c) SST $k - \omega$ with a bifurcation model, without DS_{ij}/Dt contribution



(c) SST $k - \omega$ with a bifurcation model, without DS_{ij}/Dt contribution



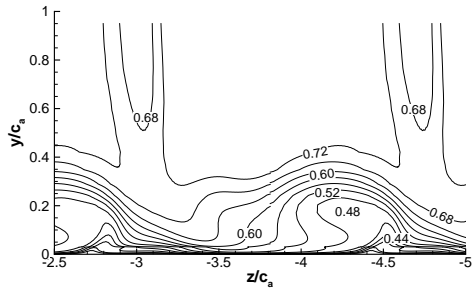
(d) Experimental data



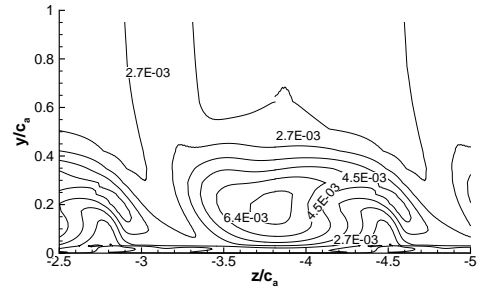
(d) Experimental data

Figure 2.33 Velocity contours

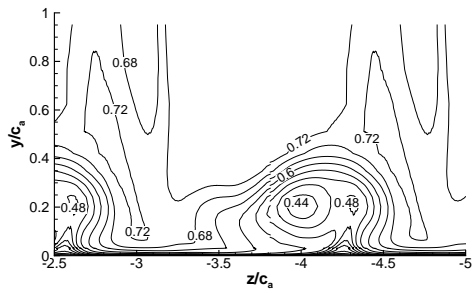
Figure 2.34 TKE contours at $X/C_a = 2.062$



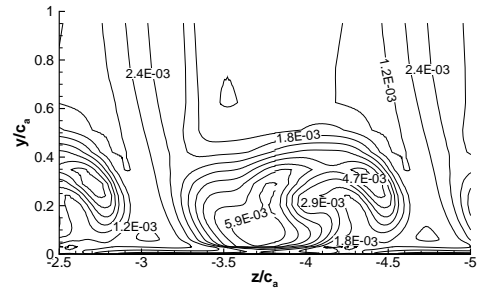
(a) SST $k - \omega$



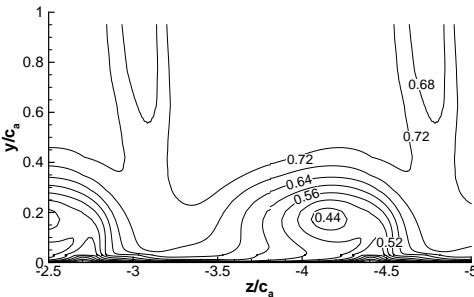
(a) SST $k - \omega$



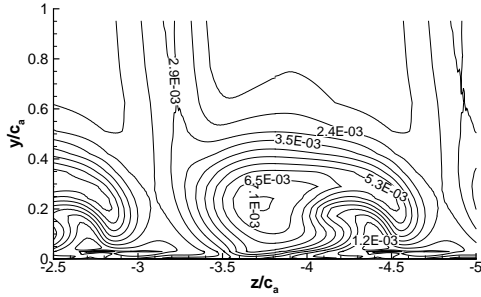
(b) SST $k - \omega$ with a bifurcation model



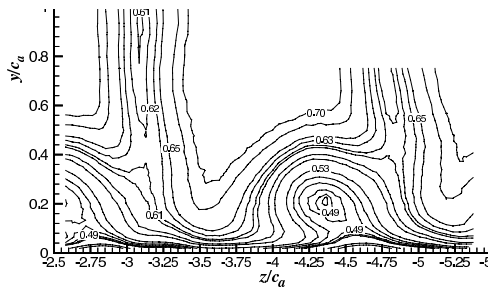
(b) SST $k - \omega$ with a bifurcation model



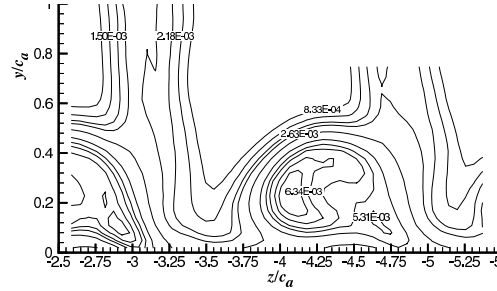
(c) SST $k - \omega$ with a bifurcation model, without DS_{ij}/Dt contribution



(c) SST $k - \omega$ with a bifurcation model, without DS_{ij}/Dt contribution



(d) Experimental data



(d) Experimental data

Figure 2.35 Velocity contours

Figure 2.36 TKE contours at $X/C_a = 2.831$

In turbomachinery, the existence of clearance between the blade tip and the casing is known to be a major source of unfavorable phenomena such as rotating instabilities and blockage in the flow passage. This could lead to severe performance loss and stall of axial compressors. The pressure difference between suction and pressure surfaces of the blade airfoils causes leakage flow which rolls up into tip leakage vortex. At the core of the vortex, the flow is laminar due to the curvature induced suppression of turbulence. Accurate prediction of the turbulence levels at the core of the vortex determines the evolution of the leakage vortex downstream of the blade trailing edge.

Muthanna (1998) have conducted experiments for the linear cascade of GE rotor B airfoil at a chord based Reynolds number of 4×10^5 and with different tip gap sizes. The end wall is stationary. It is well known that the standard RANS models produce inaccurate results for this problem (Khorrami et al., 2001; Garbaruk et al., 2005). We use this case to test the effectiveness of the rotation/curvature correction in predicting the vortex evolution accurately. The physical parameters used in the simulation are given table 2.5.

The grid generation for this case is not trivial. We use a combination of H and O topologies to generate a grid which has about 3 Million points (see Fig.2.28). A no-slip wall boundary condition is imposed on the stationary bottom wall. At the inflow, a profile extracted from a precursor boundary layer simulation consistent with the experiments is used. The top boundary is treated as a slip wall. Periodicity is imposed in the spanwise direction and atmospheric pressure is specified at the outflow.

The vortex evolution obtained with and without curvature correction are shown in Fig.2.29. The isosurfaces of Q -criterion shows the vortex core location and its movement inside the blade passage. The width of the core predicted by SST $k - \omega$ is clearly larger than that by the bifurcation model. It means that the vortex diffuses quickly if the curvature effects are not accounted.

Looking at the contours plotted in Fig.2.30, the curvature correction reduces the eddy

viscosity levels at the core of vortex. But, SST $k - \omega$ predicts unphysically large eddy viscosity levels even inside the core. Interestingly, curvature model is active even in the blade passage as well. It could be due to the camber of the blade.

The detailed comparison at different axial locations of the velocity and TKE contours (see Figs.2.31-2.36) shows that the curvature correction improves the prediction of vortex evolution over the base turbulence model. At the location $X/C_a = 1.366$, the differences in the velocity levels are small. But, the location of the vortex core is accurate with a curvature correction without accounting for DS_{ij}/Dt contribution. Similar observations can be made at the downstream locations as well. Some details of the complicated vortical system like secondary vortex are captured accurately with a curvature correction.

CHAPTER 3. GENERATING INFLOW TURBULENCE FOR EDDY SIMULATION OF TURBOMACHINERY FLOWS

3.1 Abstract

Numerical simulations of spatially developing turbulent boundary layers require specification of realistic, coherent series of time-varying velocity components at the inflow. In this work, the widely used recycling and rescaling method of generating inflow turbulence has been explored for the large eddy simulation of turbomachinery flows. To avoid the spurious linking of spanwise structures and error accumulation, a mirroring method proposed in the literature has been adopted. A computational framework is developed within an existing LES module in OpenFOAM and preliminary validation is carried out. This framework can potentially be used for eddy simulations of spatially developing boundary layers as well as turbomachinery internal flows with a specific boundary layer thickness at the inflow boundary.

3.2 Introduction

Numerical simulations of fully developed, time-evolving flows (For example: channel flow) are often performed using periodic boundary conditions in which the downstream flow can be directly re-applied at the inlet. However, these boundary conditions are not appropriate for spatially developing flows, such as turbulent boundary layers. In

simulating such flows, the flow downstream is highly dependent on the conditions at the inlet, making it necessary to specify a realistic time series of turbulent fluctuations that are in equilibrium with the mean flow. The inflow data should satisfy the Navier-Stokes equations to be accurate.

The most straightforward approach to simulate a spatially developing turbulent boundary layer is to start the calculation far upstream with a laminar profile plus random disturbances and then allow a natural transition to turbulence to occur. This method is not generally applicable for turbulent simulations as it requires a long development section to simulate natural transition and hence is prohibitively expensive.

The other simple procedure for specifying turbulent inflow conditions is to superimpose random fluctuations on a desired mean velocity profile. The amplitude of the turbulent fluctuations can be adjusted to satisfy a desired set of one-point second order statistics. However, the velocity derivative skewness is zero and hence inflow condition is void of nonlinear energy transfer and the flow lacks realistic turbulent structure. Also, a fairly lengthy development section is required, to allow for the development of organized turbulent motion. In addition, it is often hard to control the skin friction and integral boundary layer thickness at the end of the development section.

The method of using an auxiliary simulation to generate inflow boundary conditions (Akselvoll and Moin, 1995) is commonly used for internal flows. A similar approach can be used for turbulent boundary layers as well. To account for spatial growth, Spalart (1988) developed a method by adding source terms to the Navier-Stokes equations. This method is capable of producing equilibrium turbulent boundary layers with direct control on skin friction and integral boundary layer thickness. However, it requires a coordinate transformation that minimizes the streamwise inhomogeneity and hence cannot be adopted into general purpose CFD codes.

Lund et al. (1998) proposed a simplified approach in which the velocity at the inflow plane is estimated using the flow downstream. The velocity field extracted at a down-

stream location is rescaled and reintroduced at the inlet. This method proved to be very successful in generating accurate inflow data with specific boundary layer thickness. The advantage of this method is that the spatially evolving simulation itself generates its own inflow data obviating the need to store the entire time series data. Recently, Spalart et al. (2006) proposed a modification to this method without the need of using scaling formulas. For a detailed review of different inflow generation methods for LES, see Keating et al. (2004).

Some of the numerical issues reported in the literature with the Lund et al. (1998) method are: spurious spanwise structures are recycled that can grow in time and disrupt the numerical stability, sensitivity to the initialization. Spalart et al. (2006) propose to use a spanwise shift before applying the recycled data at the inlet to disorganize spurious spanwise structures. Jewkes et al. (2011) proposed a mirroring method to avoid this issue wherein the rescaled data is mirrored in the spanwise direction before applying at the inlet. Liu and Pletcher (2006) used a dynamic recycling procedure to reduce the start-up transient and to maintain a short inlet buffer zone. Lund et al. (1998) commented that it is advantageous to control the momentum thickness with a little extra effort, instead of using 99% boundary layer thickness. With that motivation, Jewkes et al. (2011) used displacement thickness in their methodology.

In this work, the recycling and rescaling method of Lund et al. (1998) and its variant proposed by Spalart et al. (2006) are implemented along with the modifications adopted from Jewkes et al. (2011). The computational framework developed within OpenFOAM is tested on large eddy simulation of flat plate boundary layer simulations as well as internal flows such as flow through plane channel and flow through annulus to validate the implementation. Then, the method is applied for large eddy simulation of turbine transition duct to demonstrate the effectiveness of the method. Preliminary results obtained from this work are discussed in the subsequent sections.

3.3 Recycling and rescaling method

In this method (Lund et al., 1998), the velocity field is first decomposed into a mean and fluctuating parts. The mean is obtained by averaging in the spanwise direction and in time. The velocity fluctuations are then defined as:

$$u'_i(x, y, z, t) = u_i(x, y, z, t) - U_i(x, y) \quad (3.1)$$

where x, y, z denote streamwise, wall-normal and spanwise directions and u, v, w are the corresponding the velocity components respectively.

The scaling laws are applied to the mean and fluctuations separately. The mean flow is rescaled according the law of the wall in the inner region and defect law in the outer region. This relates the streamwise velocity at the inflow and recycle station as:

$$U_{inlt}^{inner} = \gamma U_{recy}(y_{inlt}^+) \quad (3.2)$$

$$U_{inlt}^{outer} = \gamma U_{recy}(\eta_{inlt}) + (1 - \gamma)U_\infty \quad (3.3)$$

$$\gamma = \left(\frac{u_{\tau, inlt}}{u_{\tau, recy}} \right) \quad (3.4)$$

where y_{inlt}^+ and η_{inlt} are the inner and outer coordinates of the grid nodes at the inlet station. So, $U_{recy}(y_{inlt}^+)$ is the mean velocity at the recycle station expressed as a function of the inner coordinate at the inlet. This is obtained using linear interpolation. A similar interpolation is required for the outer coordinate as well.

The mean vertical velocity in the inner and outer regions are scaled according to

$$V_{inlt}^{inner} = V_{recy}(y_{inlt}^+) \quad (3.5)$$

$$V_{inlt}^{outer} = V_{recy}(\eta_{inlt}) \quad (3.6)$$

and the velocity fluctuations are scaled as

$$(u'_i)_{inlt}^{inner} = \gamma (u'_i)_{recy}(y_{inlt}^+, z, t) \quad (3.7)$$

$$(u'_i)_{inlt}^{outer} = \gamma (u'_i)_{recy}(\eta_{inlt}, z, t) \quad (3.8)$$

A composite profile that is valid over the entire layer is obtained by forming a weighted average of the inner and outer profiles:

$$(u_i)_{inlt} = [(U_i)_{inlt}^{inner} + (u_i')_{inlt}^{inner}][1 - W(\eta_{inlt})] + [(U_i)_{inlt}^{outer} + (u_i')_{inlt}^{outer}]W(\eta_{inlt}). \quad (3.9)$$

The weighting function $W(\eta)$ is defined as

$$W(\eta) = \frac{1}{2} \left(1 + \tanh \left[\frac{\alpha(\eta - b)}{(1 - 2b)\eta + b} \right] / \tanh(\alpha) \right) \quad (3.10)$$

where $\alpha = 4$ and $b = 0.2$.

The rescaling operation requires the scaling parameters u_τ and δ both at the recycle station and at the inlet. These are calculated at the recycle station using the data extracted and must be specified at the inlet boundary. By fixing δ at the inlet and computing u_τ using

$$u_{\tau,inlt} = u_{\tau,resc} \left(\frac{\theta_{resc}}{\theta_{inlt}} \right)^{1/[2(n-1)]}, \quad n = 5, \quad (3.11)$$

where θ is the momentum thickness.

A simple running average is used to compute the mean velocity field. But, to eliminate the starting transients, averaging is performed with a weight that decreases exponentially backward in time. The following formula achieves this:

$$U^{n+1} = \frac{\Delta t}{T} \langle u^{n+1} \rangle_z + \left(1 - \frac{\Delta t}{T} \right) U^n \quad (3.12)$$

where Δt is the computational time step, T is the characteristic time scale of the averaging interval and $\langle \rangle_z$ denotes averaging in the spanwise direction. In the beginning of the simulation, $T = 10\delta/U_\infty$ is used to eliminate the transients and as the flow starts to equilibrate, a few hundred inertial times (δ/U_∞) is used to stabilize the statistics and then a simple running average is used ($T = T_0 + t - t_0$, where t is the current time, t_0 is the time at which running average was initiated, and T_0 is the value of the interval used prior to t_0).

3.3.1 Simplified method with modifications due to Spalart *et al.* (2006)

Spalart et al. (2006) proposed a much simpler approach based on the following physical arguments:

- The near-wall turbulence regenerates itself much faster than the outer region turbulence \rightarrow Apply outer layer scaling throughout.
- When the recycling station is located quite close to the inflow, which is desirable in terms of computing cost, the conflict between inner and outer region scaling essentially vanishes \rightarrow Short recycling distance
- Corrections to the wall normal velocity component v have very little effect \rightarrow Omitted

So, the streamwise velocity at the recycling station and inlet are related as

$$u(x, y, z, t)_{inlt} = u\left(x, y \frac{\delta_{recy}}{\delta_{inlt}}, z, t\right)_{recy} \quad (3.13)$$

As it can be observed, there is no need to decompose the velocity field in this approach. A linear interpolation is used to apply the extracted velocity field at the inlet boundary.

Spalart et al. (2006) also proposed to introduce a spanwise shift while applying the recycled data at the inlet. This is to disorganize any durable spanwise structures which would otherwise be recycled and might take much longer to be damped by the spanwise diffusion. However, in the present work mirroring method proposed by Jewkes et al. (2011) is used for this purpose.

3.3.2 Modifications due to Jewkes *et al.* (2011)

The following are the modifications adopted from Jewkes et al. (2011):

- Using boundary layer displacement thickness in place of 99% thickness \rightarrow Calculating 99% thickness is not straightforward as the edge of the boundary layer is difficult to locate.

- Periodic spanwise boundary conditions were applied to disrupt the spurious linking of structures by mirroring the inlet plane.

From the rescaled inlet velocity field, mirroring method gives

$$u(y, z, t)_{mirror, inlt} = u(y, W - z, t)_{inlt} \quad (3.14)$$

$$v(y, z, t)_{mirror, inlt} = v(y, W - z, t)_{inlt} \quad (3.15)$$

$$w(y, z, t)_{mirror, inlt} = -w(y, W - z, t)_{inlt} \quad (3.16)$$

where W is the domain width. Note that w has to be negative to ensure spatial coherence once mirrored.

These modifications were applied for both Lund et al. (1998) and Spalart et al. (2006) versions of the recycling and rescaling inflow turbulence generation method. A brief flow chart for this algorithm is presented in figure 3.1.

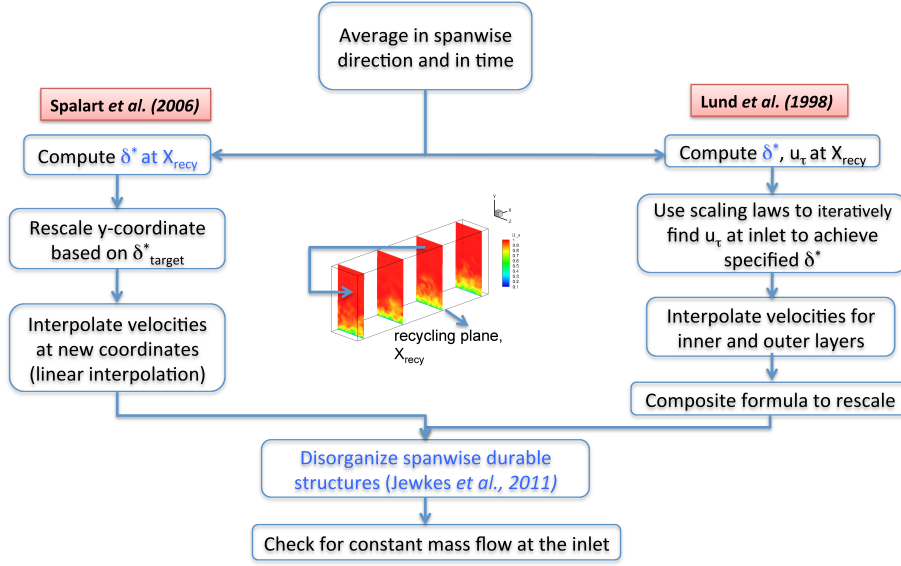


Figure 3.1 Flow chart of inflow turbulence generation algorithms

The above methods are implemented within the existing OpenFOAM LES framework. The validation studies are discussed in the following section.

3.4 Validation

The numerical algorithm used for LES in OpenFOAM is discussed in detail in the thesis of de Villiers (2006). In our current work, the dynamic Smagorinsky model is used for the subgrid scale stresses. A second order, backward, implicit scheme for time discretization and a second order central scheme (with filtering for high-frequency ringing) for spatial discretization is used.

3.4.1 Flat plate boundary layer

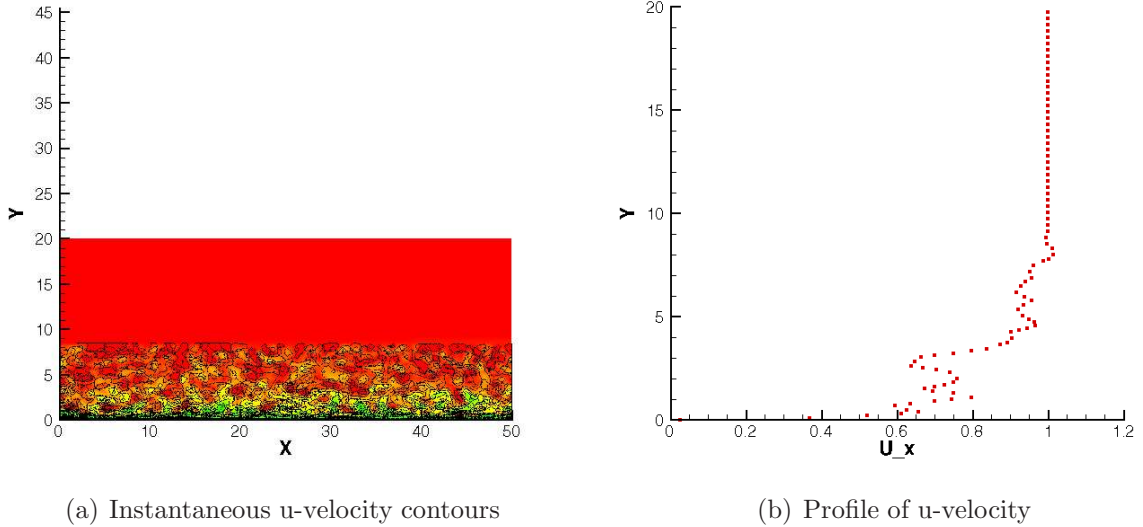


Figure 3.2 Initialization for flat plate boundary layer simulation

To validate the implementation, a spatially developing boundary layer over flat plate is simulated at a Reynolds number based on momentum thickness (θ) and freestream velocity (U_∞) of $Re_\theta = 1490$. The simulation domain has dimensions $6\delta_0 \times 3\delta_0 \times (\pi/2)\delta_0$ with corresponding grid density of $100 \times 45 \times 64$ points in the streamwise, wall-normal, and spanwise directions, respectively. δ_0 is the 99% boundary layer thickness at the mid point of the domain. The recycle station is located at $2.5\delta_{inlet}$. The solution is advanced with a time step of $\Delta t \approx 0.2\nu/u_\tau^2$ and the simulation is run for about 200 inertial time

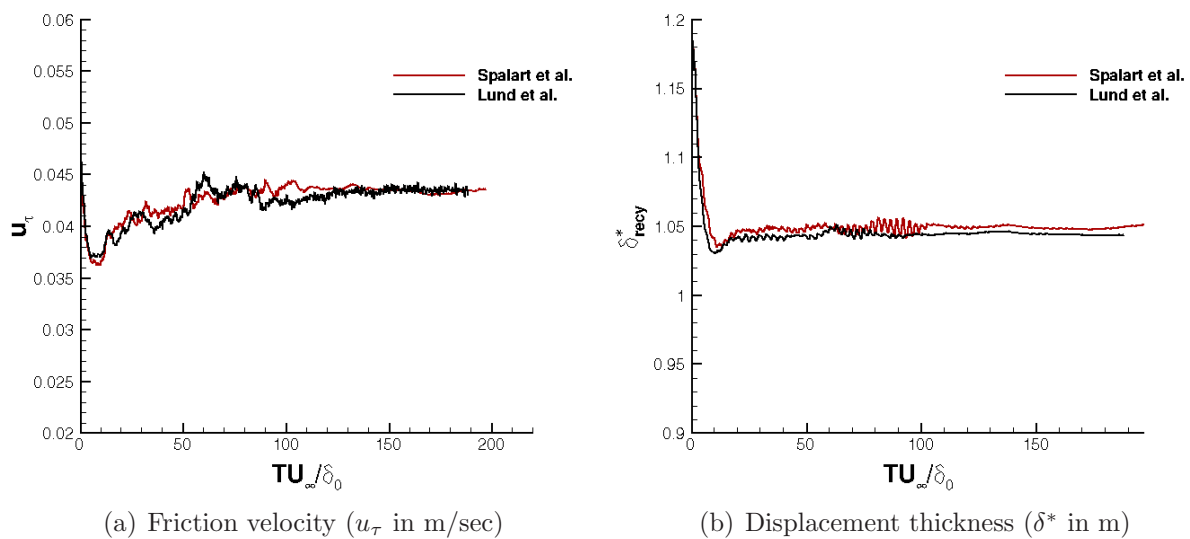


Figure 3.3 Time development of flow variables

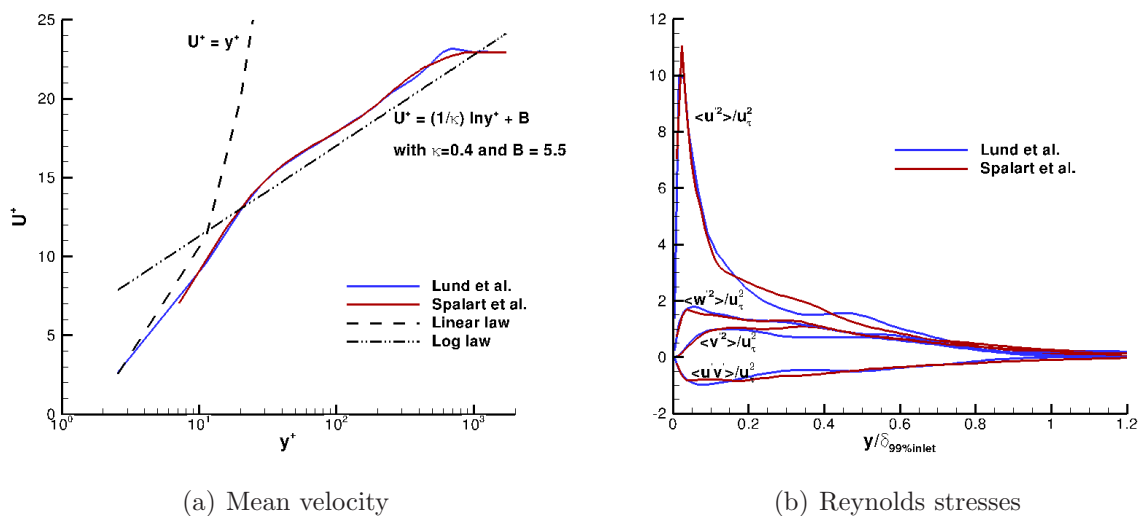
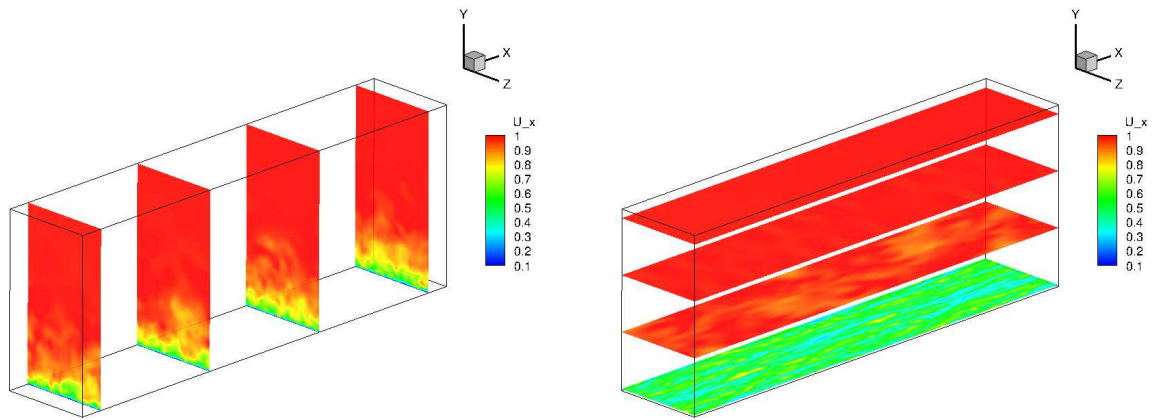


Figure 3.4 Flat plate boundary layer: one-point statistics



(a) Instantaneous velocity in X-planes

(b) Instantaneous velocity in Y-planes

Figure 3.5 Flat plate boundary layer: velocity contours

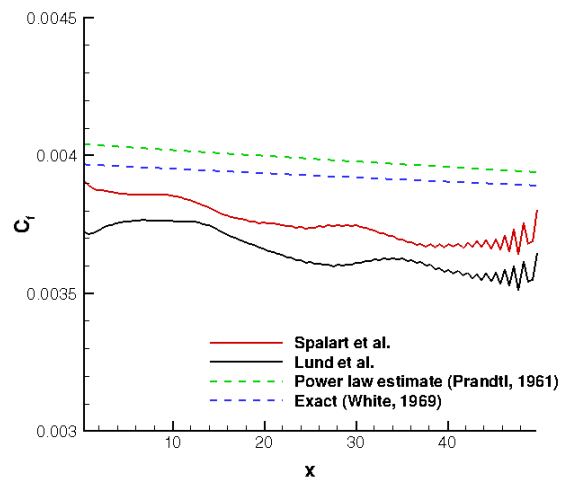


Figure 3.6 Flat plate boundary layer: Skin friction variation

scales (TU_∞/δ_0).

The mean flow is initialized using Spalding's composite law of the wall:

$$y^+ = u^+ + e^{-\kappa B} \left[e^{\kappa u^+} - 1 - \kappa u^+ - \frac{(\kappa u^+)^2}{2} - \frac{(\kappa u^+)^3}{6} \right] \quad (3.17)$$

where $y^+ = yu_\tau/\nu$ and $u^+ = u/u_\tau$. Away from the wall, $u = U_\infty$. The boundary layer growth is determined according to

$$C_f = 0.027/Re_x^{1/7}; \quad \delta_{99\%} = 0.16x/Re_x^{1/7}; \quad Re_x = U_\infty x/\nu; \quad u_\tau = \sqrt{\frac{1}{2}U_\infty^2 C_f} \quad (3.18)$$

The fluctuations are initialized such that the maximum is at around $y/\delta_{99\%} = 0.05$ and progressively die away towards the outer layer. The sample contours and velocity profile of the instantaneous velocity is presented in the figure 3.2. Such a careful initialization is important when using the recycling and rescaling method for inflow conditions and it is recognized in the literature as well (Spalart et al., 2006).

The time evolution of the friction velocity and the boundary layer displacement thickness is shown in figure 3.3. It can be observed that it takes about 50 inertial time scales for the transients to die and the solutions to become stable. The friction velocity decreases initially and if the initialization is not careful, the flow might become laminar. But, with our initialization it can be observed that the friction velocity increases and reaches a stable value after about 100 inertial time scales. A similar trend can be seen in the displacement thickness as well.

The statistics, mean velocity and the Reynolds stresses obtained are plotted in figure 3.4. The mean velocity profile clearly shows the presence of log-law, although the intercept of the log layer is slightly higher than the standard value. The Reynolds stress plot shows that the streamwise normal stress is dominant. In both figure 3.3 and 3.4, Lund et al. (1998) is compared with a modified version proposed by Spalart et al. (2006). The two methods gave similar results.

Slices taken in the X and Y planes are shown in figure 3.5 to demonstrate the flow development downstream and the presence of streaks just above the wall. Finally, the skin

friction is plotted in figure 3.6 and is compared with the standard estimates available for the flat plate boundary layers. The skin friction variation is consistent with the estimates, but near the outflow boundary the results show unphysical oscillations. This issue will be addressed in the subsequent section.

3.4.2 Flow through channel

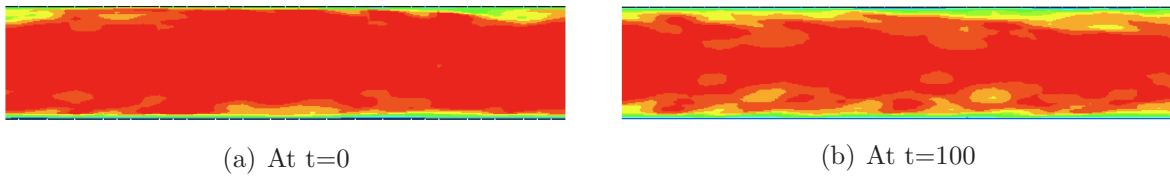
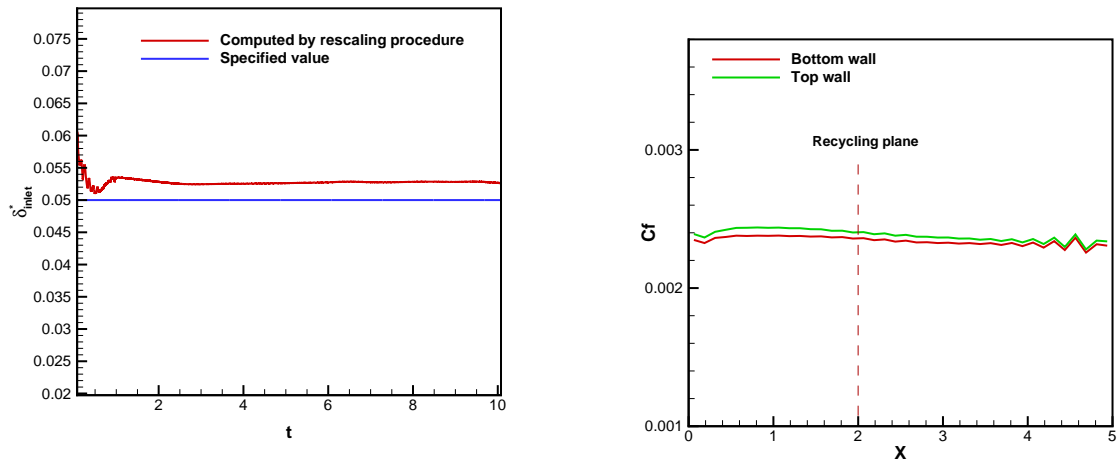


Figure 3.7 Flow through plane channel: Instantaneous velocity contours



(a) Time history of the displacement thickness at inlet. The error between the computed and specified value is less than 5%

(b) Skin friction variation along both the walls

Figure 3.8 Flow through plane channel

As a next step, the recycling and rescaling algorithm is extended for flow through a channel. The modifications and assumptions used in the algorithm are:

- The cell list at the recycle station is indexed so as to allow for spanwise averaging as well as computing boundary layer displacement thickness on both the walls.

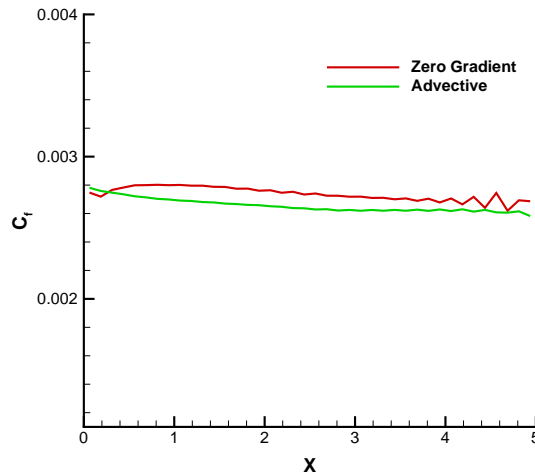


Figure 3.9 Channel flow: Skin friction variation with different outflow boundary conditions

- It is assumed that the velocity at the center of the channel is the freestream velocity.

In figure 3.7, the velocity contours are plotted at time $t=0$ and $t=100$ and it can be observed that the boundary layer thickness adjusts according to the inflow specifications. The time evolution of the displacement thickness is plotted in 3.8. The plotted skin friction shows that the variation is similar on both the bottom and top walls and that there are unphysical oscillations near the outflow boundary similar to that observed in the flat plate boundary layer problem.

When the outflow boundary condition is changed from the zero gradient condition to the advective outflow boundary condition, the unphysical behavior near the outflow boundary is reduced. This is shown in figure 3.9.

3.4.3 Flow through annulus

Before using this methodology for the turbomachinery flows, it is tested on flow through an annulus. This requires the following modifications/assumptions:

- Using radial coordinate instead of Y-coordinate.

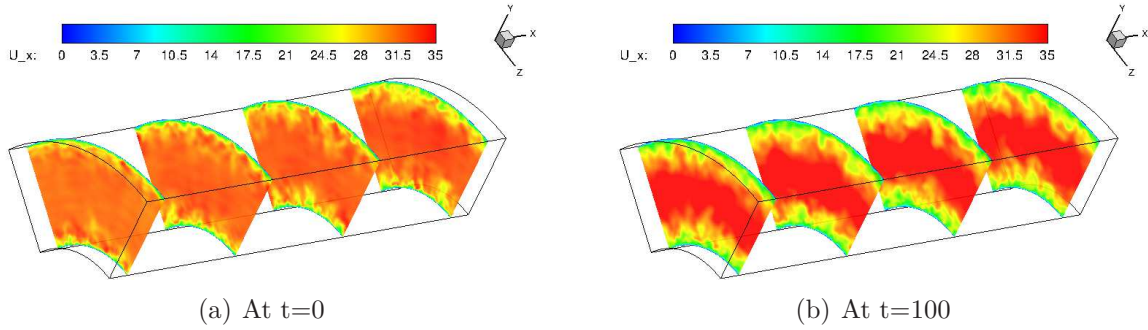


Figure 3.10 Flow through annulus: Instantaneous velocity contours

- Effect of transverse curvature is assumed negligible for the inflow generation purpose.

The results from the tests performed on flow through annulus are plotted in figure 3.10 at two different instants of time. The adjustment of boundary layer thickness according to the inflow specification is demonstrated.

3.4.4 Turbine transition duct

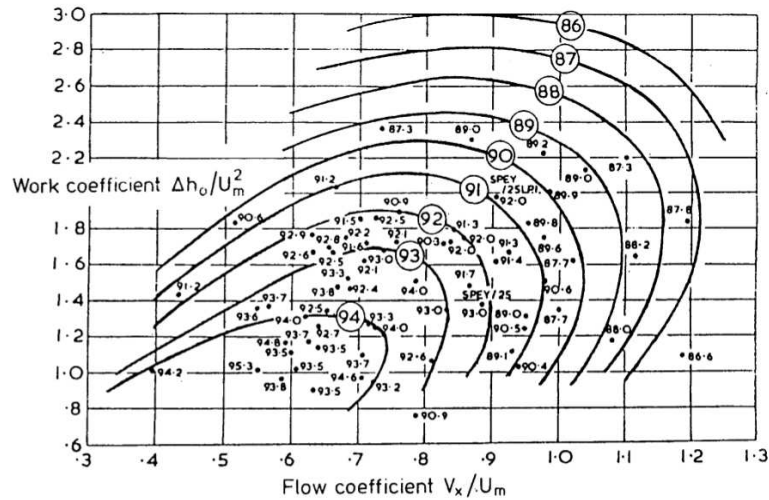


Figure 3.11 Smith's chart: Turbine efficiency curves

A turbine transition duct constitutes the flow path between the high pressure turbine (HPT) and low pressure turbine (LPT) of a high-bypass ratio turbofan engine. It is instructive to look at Smith's chart shown in figure 3.11 to understand the purpose of

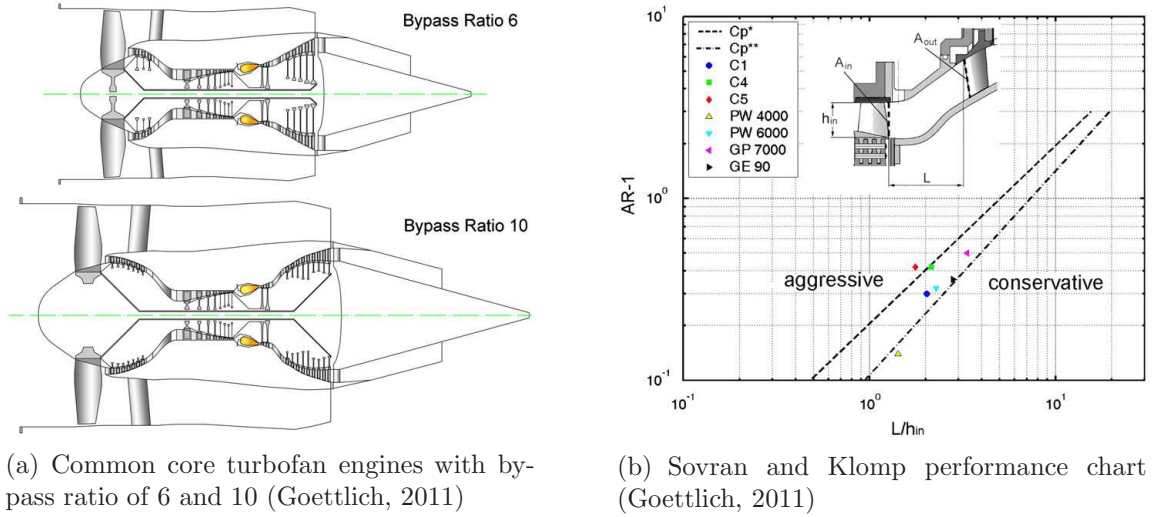


Figure 3.12 Current trends in the turbofan engines

the transition duct in a turbofan engine. The work coefficient (ψ) and flow coefficient (ϕ) of a turbine are defined as

$$\psi = \frac{C_P \Delta T_{0S}}{U^2/2} \quad (3.19)$$

$$\phi = C_a/U; \quad U_m = 2\pi N r_m \quad (3.20)$$

where C_P is the heat capacity at constant pressure, T_{0S} is the stagnation temperature drop, C_a is the axial velocity, U is the blade velocity, N is the rpm and the subscript m denotes the meanline quantities. The turbine transition duct

- Takes the flow from a lower radius (HPT) to a higher radius (LPT) $\rightarrow U_m$ increases \rightarrow Stage loading (work) coefficient decreases.
- Diffuses the flow (C_a decreases) \rightarrow Flow coefficient decreases.

From Smith's chart, reduced ψ and ϕ gives higher turbine efficiency and hence fewer stages are required for the same work output. This results in reduced weight of the engine. As the LPT accounts for 20–30% of the overall engine weight, even 1% reduction in weight can lead to 5% increased payload and hence can have a huge impact on the

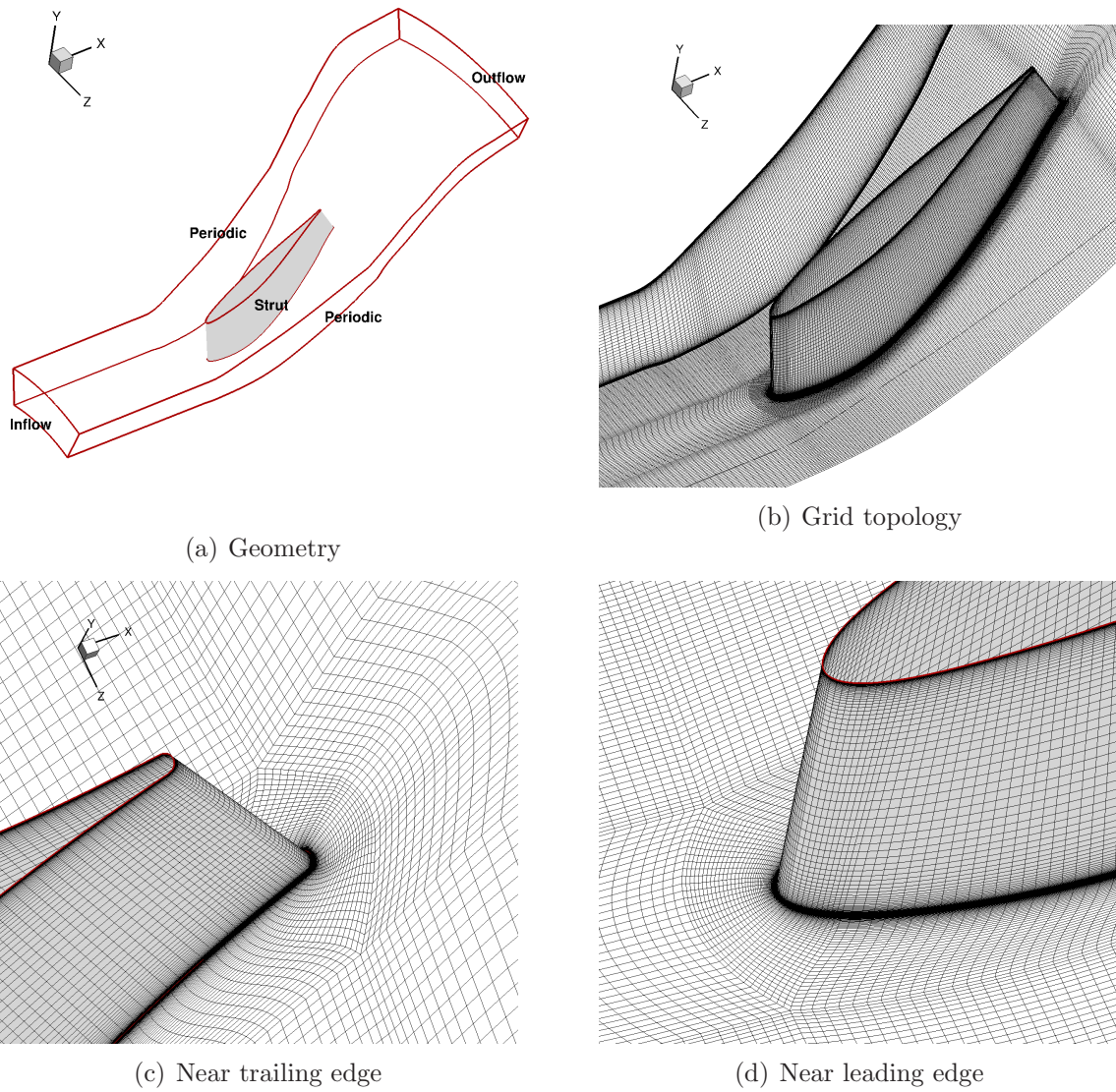


Figure 3.13 Flow configuration of the turbine transition duct

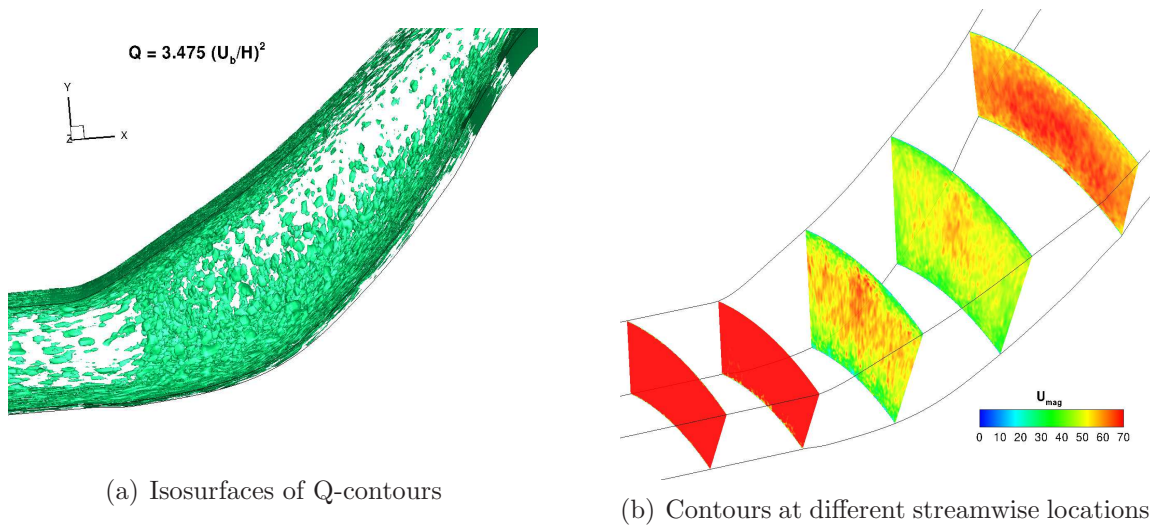


Figure 3.14 Flow through transition duct without struts

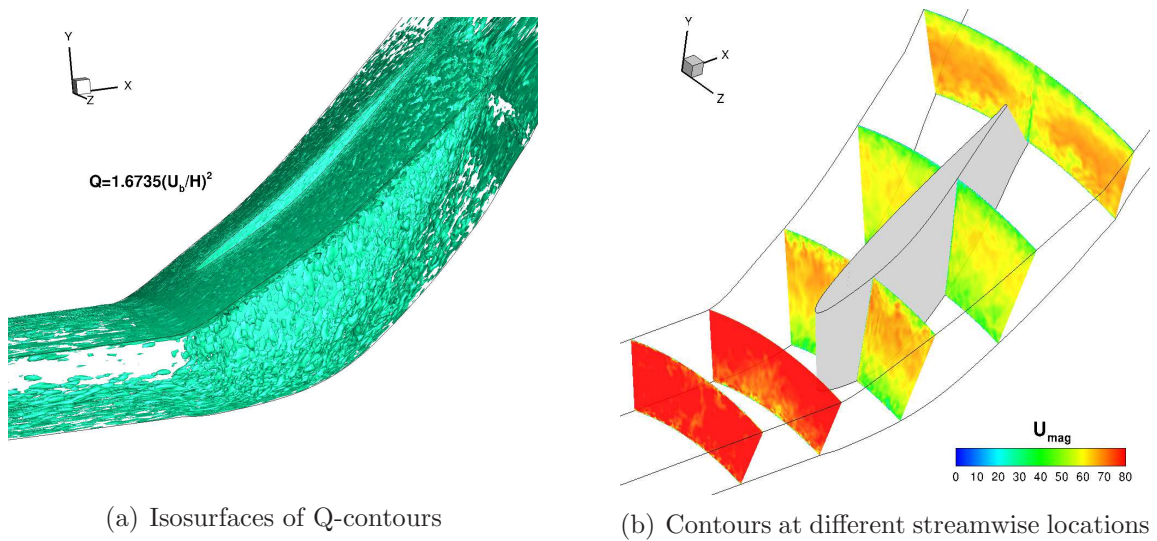


Figure 3.15 Flow through transition duct with struts

operating profit. The current trends in the aero engines is towards higher and higher bypass ratios. As shown in the figure 3.12, when the bypass ratio is increased from 6 to 10 assuming a common core, the duct between the HPT and LPT becomes longer and steeper adding to the overall weight of the engine. To avoid excessive increase in weight, the ducts have to be designed as short as possible and that poses severe challenges to the designers due to the possibility of flow separation.

So, the objective of current work is to study the detailed flow physics in turbine transition duct and evaluate the scalar turbulence models that are used in the design process of this components. The LES data can be used to potentially refine the turbulence models, if found necessary. In this report, however, the discussion is limited to validation of the inflow turbulence generation method.

The flow configuration and the grid generated for the turbine transition duct (30° sector) are shown in figure 3.13. The grid has about 5 Million points with a combination of H and O topologies. As shown in figure 3.14, isosurfaces of Q-contours reveal the turbulent structures near the hub and casing. As the flow passes through the duct, the boundary layer on the hub thickens due to concave curvature and hence, more structures are observed in that region. This is consistent with the color contours of the velocity magnitude. The flow diffuses as it reaches the exit of the duct and hence the magnitude of the velocity increases. When struts are present, the strut diffusion is also present in addition to the duct diffusion. The isosurfaces of Q-contours presented in 3.15 show that the turbulent structures near the inflow.

3.5 Future scope of work

3.5.1 Algorithm enhancements

- Prescribing Reynolds stress tensor and energy spectra (Ferrante and Elghobashi, 2004)

- Investigate specification of freestream turbulence intensity to study transitional flows
- Modifications to specify realistic wake profile at the inflow boundary

3.5.2 Applications

- Further work on LES of turbine transition to understand the influence of struts; influence of wakes, swirl etc.
- To investigate tip leakage flow where the inflow has a specific momentum thickness Reynolds number (You et al., 2007).

Note that, this inflow turbulence generation method can also be used for Improved Delayed Detached Eddy Simulation (IDDES).

CHAPTER 4. GENERAL CONCLUSIONS

4.1 Modeling rotation and curvature effects within scalar eddy viscosity model framework

Simple models for rotation and curvature effects were proposed based on bifurcation analysis in rotating homogeneous shear flow. They are parameterized as a function of η_3 . Extensive validation has been carried out to test the proposed models and to compare the bifurcation approach and the modified coefficients approach. The results obtained using these models are encouraging in all the test cases.

Two approaches of implementing material derivative of strain rate tensor are discussed: Eulerian and Lagrangian. They are tested on simple flows in which curvature is known *a priori*. Lagrangian approach is computationally expensive due to interpolation and moreover, Eulerian approach is easier to implement.

The η_3 based model proposed in the modified coefficients approach is competitive with the bifurcation based models in all the cases tested. In the rotating channel and rotating backstep cases, it performs better than Br based model proposed by Hellsten in responding appropriately to the imposed system rotation.

The derivation of the new model in the bifurcation approach is guided by the equilibrium analysis and hence can be thought of as a “physics based” model which is more reliable for use in the industrial design process. And hence, this model is tested on challenging engineering applications. Accurate prediction of combined rotation and curvature effects still remains a challenge for the models. Both at low and high Reynolds

numbers, only a qualitative agreement is obtained for the rotating curved ducts. In the circulation control airfoil case, curvature correction improved the lift prediction. The suction peak is not predicted accurately. But, that is not relevant to the curvature effects. In tip clearance flow, the evolution of the leakage vortex is predicted accurately by the curvature correction model. Interestingly, accurate results were obtained even without DS_{ij}/Dt contribution. Note that when DS_{ij}/Dt is not used, η_3 in the bifurcation model is similar to the Q -criterion of detecting the vortex core. Hence, this observation can be generalized for all vortical flows.

4.2 Generating inflow turbulence for eddy simulation of turbomachinery flows

A computational framework is developed to generate inflow turbulence for eddy simulation of turbomachinery flows. The widely used recycling and rescaling method along with recently proposed modifications is implemented and systematically validated. The accuracy of the method is tested on spatially developing boundary layer over flat plate by comparing the skin friction variation with that using correlations in the literature. The extension of the inflow generation method to flow through a channel and flow through an annulus are briefly discussed. The effectiveness of the computational framework is demonstrated with the large eddy simulation of turbine transition duct.

BIBLIOGRAPHY

- Akselvoll, K., Moin, P., 1995. Large eddy simulation of turbulent confined coannular jets and turbulent flow over a backward facing step. Report tf-63, Stanford University, Stanford, CA 94305.
- Arolla, S. K., Durbin, P. A., 2013a. Modelling rotation and curvature effects within scalar eddy viscosity model framework. *Int. J. Heat Fluid Flow*. 39, 78–89.
- Arolla, S. K., Durbin, P. A., January 2013b. Assessing the effects of streamline curvature on the aerodynamics of circulation control airfoil. AIAA Paper 2013-0958.
- Arolla, S. K., Durbin, P. A., June 2012a. Incorporating rotation and curvature effects in scalar eddy viscosity closures. AIAA Paper 2012-3283.
- Arolla, S. K., Durbin, P. A., 2012b. On the numerical implementation of a rotation/curvature correction for turbulence models in a finite volume CFD code, In Preparation.
- Barlow, R. S., Johnston, J. P., 1988. Structure of a turbulent boundary layer on a concave surface. *J. Fluid Mech.* 191, 137–176.
- Barri, M., Andersson, H. I., 2010. Turbulent flow over a backward-facing step. part 1. effects of anti-cyclonic system rotation. *J. Fluid Mech.* 665, 382–417.
- Boysan, F., Ewan, B. C., Swithenbank, J., Ayers, W. H., 1983. Experimental and theoretical studies of cyclone separator aerodynamics. IChemE Symposium Series No, 69, 305–320.

- Cazalbou, J., Chassaing, P., Dufour, G., Carbonneau, X., 2005. Two-equation modeling of turbulent rotating flows. *Phys. Fluids* 17, 1–14.
- Cheah, S., Iacovides, H., Jackson, D., Ji, H., Launder, B., 1996. LDA investigation of the flow development through rotating U-ducts. *J. Turbomach.* 118 (3), 590–596.
- Dhakal, P. T., Walters, K. D., 2011. A three-equation variant of the SST $k - \omega$ model sensitized to rotation and curvature effects. *J. Fluids Eng.* 133.
- Duraisamy, K., Iaccarino, G., 2005. Curvature correction and application of the $v^2 - f$ turbulence model to tip vortex flows. In: *Annual Research Briefs*. Center for Turbulence Research, Stanford University.
- Durbin, P. A., 1993. A Reynolds stress model for near-wall turbulence. *J. Fluid Mech.* 249, 465–498.
- Durbin, P. A., 2011. Review: Adapting scalar turbulence closure models for complex turbulent flows. *J. Fluids Eng.*
- Durbin, P. A., Medic, G., 2007. *Fluid dynamics with a computational perspective*. Cambridge University Press, New York.
- Durbin, P. A., Petterson-Reif, B. A., 1999. On algebraic second moment models. *Flow, Turbul. and Combust.* 63 (23-37).
- Durbin, P. A., Petterson-Reif, B. A., 2010. *Statistical theory and modeling for turbulent flows*, 2nd Edition. John Wiley and Sons, New York.
- de Villiers, E., July 2006. The potential of large eddy simulation for the modelling of wall bounded flows. Ph.D. thesis, Imperial college of science.
- Garbaruk, A., Shur, M. L., Strelets, M., Travin, A., July 2005. Detached-eddy simulation of a linear compressor cascade with tip gap and moving wall. *Symposium on Hybrid RANS-LES Methods*.

- Gatski, T. B., Jongen, T., 2000. Nonlinear eddy viscosity and algebraic stress models for solving complex turbulent flows. *Prog. Aerosp. Sci.* 36 (655-682).
- Gillis, J., Johnston, J. P., Kays, W. M., Moffat, R. J., 1980. Turbulent boundary layer on a convex curved surface. Ph.D. thesis, Dept. Mech. Eng., Stanford University.
- Girimaji, S., 1997. A Galilean invariant explicit algebraic Reynolds stress model for turbulent curved flows. *Phys. Fluids* 9 (4).
- Goettlich, E., 2011. Research on the aerodynamics of intermediate turbine diffusers. *Prog. Aerosp. Sci.* 47 (4), 249–279.
- Grundestam, O., Wallin, S., Johansson, A. V., 2008. Direct numerical simulations of rotating turbulent channel flow. *J. Fluid Mech.* 598, 177–199.
- Guleren, K., Turan, A., 2007. Validation of large-eddy simulation of strongly curved stationary and rotating U-duct flows. *Int. J. Heat Fluid Flow* 28, 909–921.
- Ferrante, A., Elghobashi, S. E., 2004. A robust method of generating inflow conditions for direct simulations of spatially-developing turbulent boundary layers. *J. Comput. Phys.* 198 (372).
- Hellsten, A., 1998. Some improvements in Menter's $k - \omega$ SST turbulence model. AIAA Paper 1998-2554.
- Holloway, A. G. L., Tavoularis, S., 1989. The effects of curvature on sheared turbulence. Ph.D. thesis, University of Ottawa.
- Howard, J. H. G., Patankar, S. V., Bordyniuk, R. M., 1980. Flow prediction in rotating ducts using coriolis-modified turbulence models. *J. Fluids Eng.* 102, 456–461.
- Iacovides, H., Launder, B. E., Li, H. Y., 1996. The computation of flow development through stationary and rotating u-ducts of strong curvature. *Int. J. Heat Fluid Flow* 17, 22–33.

- Jewkes, J., Chung, Y., Carpenter, P., 2011. Modification to a turbulent inflow generation method for boundary-layer flows. *AIAA Journal* 49 (1), 247–250.
- Johnson, P. L., Johnston, J. P., 1989. The effects of grid generated turbulence on a flat and concave turbulent boundary layers. Ph.D. thesis, Dept. Mech. Eng., Stanford University.
- Johnston, J. P., Halleen, R. M., Lezius, D. K., 1972. Effects of spanwise rotation on the structure of two-dimensional fully turbulent channel flow. *J. Fluid Mech.* 56, 533–557.
- Kalitzin, G., Medic, G., Iaccarino, G., Durbin, P. A., 2005. Near-wall behavior of RANS turbulence models and implications for near wall functions. *J. Comput. Phys.* 204, 265–291.
- Keating, A., Piomelli, U., Balaras, E., Kaltenbach, H., 2004. *A priori* and *a posteriori* tests of inflow conditions for large-eddy simulation. *Phys. Fluids* 16 (12), 4696–4712.
- Khodak, A., Hirsch, C., 1996. Second order nonlinear models with explicit effect of curvature and rotation. In: Proc. 3rd ECCOMAS Computational Fluid Dynamics Conf., Paris. pp. 690–696.
- Khorrami, M., Li, F., Choudhari, M., May 2001. A novel approach for reducing rotor tip-clearance induced noise in turbofan engines. *AIAA Paper* 2001-2148.
- Kristoffersen, R., Andersson, H. I., 1993. Direct simulations of low-reynolds-number turbulent-flow in a rotating channel. *J. Fluid Mech.* 256, 163–197.
- Laskowski, G. M., Durbin, P. A., 2007. Direct numerical simulations of turbulent flow through a stationary and rotating infinite serpentine passage. *Phys. Fluids* 18.
- Launder, B., Rodi, W., 1983. The turbulent wall jet measurements and modeling. *Annual Review of Fluid Mechanics* 15, 429–59.

- Liu, K., Pletcher, R., 2006. Inflow conditions for the large eddy simulation of turbulent boundary layers: A dynamic recycling procedure. *J. Comput. Phys.* 219, 1–6.
- Lund, T. M., Moin, P., 1996. Large-eddy simulation of a concave wall boundary layer. *Int. J. Heat Fluid Flow* 17, 290–295.
- Lund, T., X, W., Squires, K., 1998. Generation of turbulent inflow data for spatially developing boundary layer simulations. *J. Comput. Phys.* 140, 233–258.
- Menter, F. R., October 1992. Improved two-equation $k - \omega$ turbulence models for aerodynamics flows. Tech. Rep. TM-193975, NASA.
- Menter, F. R., 1993. Zonal two equation $k - \omega$ turbulence models for aerodynamic flows. AIAA Paper 1993-2906.
- Muthanna, C., November 1998. Flowfield downstream of a compressor cascade with tip leakage. Masters thesis, Virginia Polytechnic Institute, Blacksburg, Virginia.
- Nishino, T., Hahn, S., Shariff, K., 2010. Large eddy simulation of turbulent coanda jet on a circulation control airfoil. *Phys. Fluids* (22 125105).
- Pettersson-Reif, B. A., Durbin, P. A., Ooi, A., 1999. Modeling rotational effects in eddy-viscosity closures. *Int. J. Heat Fluid Flow* 20, 563–573.
- Simon, T. W., Moffat, R. J., Johnston, J. P., Kays, W. M., 1982. Turbulent boundary layer heat transfer experiments: curvature effects including introduction and recovery. Tech. Rep. CR 3510, NASA.
- Slack, M. D., Prasad, R. O., Bakker, A., Boysan, F., 2000. Advances in cyclone modeling using unstructured grids. *Trans. IChemE, Part A* 78.
- Smirnov, P. E., Menter, F. R., October 2009. Sensitization of the SST turbulence model to rotation and curvature by applying the spalart-shur correction term. *J. Turbomach.* 131.

- Spalart, P. R., 1988. Direct simulation of a turbulent boundary layer up to $re_\theta = 1410$. *J. Fluid Mech.* 187 (61).
- Spalart, P. R., Shur, M. L., 1997. On the sensitization of turbulence models to rotation and curvature. *Aerosp. Sci. Technol.* 1, 297–302.
- Spalart, P. R., Strelets, M., Travin, A., 2006. Direct numerical simulation of large-eddy-break-up devices in a boundary layer. *Int. J. Heat Fluid Flow* 27, 902–910.
- Speziale, C. G., MacGiollaMhuiris, N., 1989. On the prediction of equilibrium states in homogeneous turbulence. *J. Fluid Mech.* 209, 591–615.
- You, D., Wang, M., Moin, P., Mittal, R., 2007. Large-eddy simulation analysis of mechanisms for viscous losses in a turbomachinery tip-clearance flow. *J. Fluid Mech.* 586, 177–204.
- Wallin, S., Johansson, A. V., 2002. Modelling streamline curvature effects in explicit algebraic Reynolds stress turbulence models. *Int. J. Heat Fluid Flow* 23, 721–730.